

UNIVERSIDADE DE SÃO PAULO  
ESCOLA DE ENGENHARIA DE SÃO CARLOS

LUCAS FIOCCO SCIUTI

Random laser in vitreous matrix with inhomogeneous scatterer distribution and a  
statistical approach in polymeric nanofiber random laser

São Carlos

2019



LUCAS FIOCCO SCIUTI

Random laser in vitreous matrix with inhomogeneous scatterer distribution and a statistical approach in polymeric nanofiber random laser

Dissertation presented to the Graduate Program in Materials Science and Engineering at São Carlos Engineering School, University of São Paulo, to obtain the degree of Master of Science.

Concentration area:

Development, characterization and application of materials

Advisor:

Prof. Dr. Leonardo De Boni

CORRECTED VERSION

São Carlos

2019

AUTORIZO A REPRODUÇÃO TOTAL OU PARCIAL DESTE TRABALHO, POR QUALQUER MEIO CONVENCIONAL OU ELETRÔNICO, PARA FINS DE ESTUDO E PESQUISA, DESDE QUE CITADA A FONTE.

Ficha catalográfica elaborada pela Biblioteca Prof. Dr. Sérgio Rodrigues Fontes da EESC/USP com os dados inseridos pelo(a) autor(a).

F416r      Fiocco Sciuti, Lucas  
Random laser in inhomogeneous scatterer distribution in vitreous matrix and a statistical approach in random laser polymeric nanofiber / Lucas Fiocco Sciuti; orientador Leonardo De Boni. São Carlos, 2019.

Dissertação (Mestrado) - Programa de Pós-Graduação em Ciência e Engenharia de Materiais e Área de Concentração em Desenvolvimento, Caracterização e Aplicação de Materiais -- Escola de Engenharia de São Carlos da Universidade de São Paulo, 2019.

1. Random laser. 2. Xerogel. 3. Inhomogeneous scatterers. 4. Nanofiber. 5. Pearson correlation. I. Título.

## FOLHA DE JULGAMENTO

Candidato: Bacharel **LUCAS FIOCCO SCIUTI**.

Título da dissertação: "Laser aleatório em distribuição inhomogênea de espalhadores matrizes vítreas e uma abordagem estatística em nanofibras poliméricas".

Data da defesa: 26/02/2019.

### Comissão Julgadora:

### Resultado:

Prof. Dr. **Leonardo De Boni**  
**(Orientador)**  
(Instituto de Física de São Carlos/IFSC)

Aprovado

Prof. Dr. **Marcelo Gonçalves Vivas**  
(Universidade Federal de Alfenas/UNIFAL)

Aprovado

Dr. **Daniel Souza Corrêa**  
(EMBRAPA)

APROVADO

Coordenador do Programa de Pós-Graduação em Ciências e Engenharia de Materiais:  
Prof. Associado **Rafael Salomão**

Decano da Comissão de Pós-Graduação:  
Prof. Titular **Humberto Breves Coda**



*Dedicated to my wife, parents and  
brother for all support and love.*



## ACKNOWLEDGEMENTS

The development of this thesis was only possible thanks to the collaboration of several people that I would like to express my gratitude in those lines.

First of all, I would like to thank my advisor, Prof. Dr. Leonardo De Boni for all his dedication to make me achieve my goals. He has been inspiring me through his friendship, patience, hardworking and passion. Always ready to help, give valuable advices and share lab experiences.

I would like to thank the whole Photonics Group that I am proud to be part of: Professors Dr. Cléber Renato Mendonça, Dr. Lino Misoguti, Dr. Sérgio C. Zílio, Dr. Maximo Siu Li, Dr. Luís G. Marcassa; the group staff Daniel Foschini for great support in the office and André Romero for effortless help in the lab, mainly when something was “out of control”; a special thanks for all my labmates, Gustavo, Leandro, Fernando, Flávio, Franciele, Nathália, Sabrina, Kelly, Otuka, Henry, Molíria, Jéssica, Danyellen and Juliana that somehow teach me physics stuff, lab stuff and even life stuff. My gratitude for provide me really pleasurable working days.

My acknowledgements to University of São Paulo through São Carlos Institute of Physics and São Carlos Engineering School, that has provided me high level undergrad and masters studies since 2013. Also, to the Coordenação de Aperfeiçoamento de Pesquisa de Nível Superior (CAPES) for the financial support at the masters’ scholarship.

Finally, I would like to express my eternal gratitude for my family which gave me the first education allowing me to be what I am today. A special thanks for my parents, Donizetti and Rita, that always support my objectives. For my big brother, Vinicius, that is my guideline in life. And for my amazing wife, Tássia Gonçalves, that was on my side in the hard and happy times of this work, always supporting, helping and loving. I dedicate this thesis to them.



“Science knows no country, because knowledge belongs to humanity, and is the torch which illuminates the world.”

Louis Pasteur (1822 - 1895)



## ABSTRACT

SCIUTI, L. F. **Random laser in vitreous matrix with inhomogeneous scatterer distribution and a statistical approach in polymeric nanofiber random laser.** 2019. 87 f. Dissertation (Master in Science) – São Carlos Engineering School, University of São Paulo, São Carlos, 2019.

Random laser has been shown a great alternative to applications in several technological branches such as sensors, portable and flexible devices, miniaturized lasers among others due to the random laser does not need a mirror cavity. Due to its wide utilization, it is important the searching for new materials and architectures concerning gain medium, host matrix or the scatterers and how they are distributed. In this work, we have studied the laser energy threshold dependency as a function of the scatterer center distribution in the random laser system volume for Rhodamine 6G-doped xerogel containing TiO<sub>2</sub> scatterers. So, the samples presented a higher scatterer density in one face's sample when compared to the opposite face and it was measured the energy threshold with the pumping laser hitting the sample both on the side with greater density of scatterers and on the opposite side at a time. Initially, we measured the energy threshold of 3.6  $\mu\text{J}/\text{pulse}$  for a samples without scatterer centers and we demonstrated a decreasing of 22% in the laser threshold when pumping in the lower scatterer density sample's face, and, inversely, an increasing of 85% when the pumping was done in the higher scatterer density side. This effect was attributed to the role scatterers have in each configuration. In a second part, it was studied the random laser property of two Rhodamine B-doped PMMA nanofibers samples with 1% and 5% (m/m) of dye concentration, both produced via electrospinning technique. It was applied the Pearson correlation coefficient in emission spectra to map the laser modes interaction as a function of time in coherent random laser emission, such as monitor the line widening and red/blueshift in the emission band in an incoherent random laser. This correlation method proved to be sensitive to small variations in the spectra. It was also shown the mode-locking transition between an incoherent and a coherent emission just by changing the pumping place in the sample due to different fiber densities that occurs in its fabrication and alters the scattering properties of the material.

Keywords: Random laser. Xerogel. Inhomogeneous scatterers. Nanofiber. Pearson correlation.



## RESUMO

SCIUTI, L. F. **Laser aleatório em matrizes vítreas com distribuição inomogênea de espalhadores e uma abordagem estatística em laser aleatório de nanofibras poliméricas.** 2019. 87 f. Dissertação (Mestrado em Ciências) – Escola de Engenharia de São Carlos, Universidade de São Paulo, São Carlos, 2019.

Lasers aleatórios tem se mostrado uma ótima alternativa para aplicações em vários ramos tecnológicos como sensores, dispositivos flexíveis e portáteis, lasers miniaturizados entre outros devido ao laser aleatório não necessitar de uma cavidade de espelhos. Devido a sua ampla utilização, é importante a pesquisa de novos materiais e arquiteturas acerca de meio de ganho, a matriz hospedeira ou os espalhadores e como estão distribuídas na matriz. Nesse trabalho, estudamos a dependência da energia de limiar laser como função da distribuição dos centros espalhadores no volume do sistema laser aleatório para amostras de xerogel dopados com Rodamina 6G contendo espalhadores de  $\text{TiO}_2$ . Para isso, as amostras apresentavam uma densidade de espalhadores maior em uma face quando comparada com a face oposta e era medido o limiar laser com o laser de bombeio atingindo a amostra tanto pelo lado com maior densidade de espalhadores quanto pelo lado oposto. Inicialmente, obtivemos uma energia de limiar de  $3,6 \mu\text{J/pulse}$  para uma amostra sem centros espalhadores e demonstrou-se que houve uma diminuição de 22% na energia de limiar laser quando bombeado no lado com menor densidade de espalhadores e, inversamente, um aumento de 85% quando o bombeio era feito pelo lado com maior densidade. Esse efeito foi atribuído ao papel que os espalhadores têm em cada configuração. Numa segunda parte, foi estudado a propriedade de laser aleatório de duas amostras de nanofibras de PMMA dopadas com Rodamina B com 1% e 5% (m/m) de concentração de corante, ambas produzidas via técnica de eletrofiação. Foi aplicada a correlação de coeficiente de Pearson em espectros de emissões de para mapear a interação de modos laser como função do tempo em emissões de laser aleatório coerente, assim como monitorar alargamento e red/blueshift da banda de emissão de laser aleatório incoerente. O método de correlação se mostrou sensível a pequenas variações de espectro. Também foi mostrado a transição de modos travados entre emissões coerente e incoerente apenas mudando o local de bombeio na amostra devido as diferentes densidades de fibra que ocorrem na amostra durante sua fabricação e que alteram a propriedade de espalhamento do material.

Palavras-chave: Laser aleatório. Xerogel. Espalhadores inomogêneos. Nanofibra. Correlação de Pearson.



## LIST OF FIGURES

|  |    |
|--|----|
| Figure 2.1: Diagram representing energy levels transitions such as spontaneous emission, absorption and stimulated emission.....   | 27 |
| Figure 2.2: Schematic energy levels of an organic dye. The ground and excited states have several vibrational states. The molecule quickly relaxes to a vibrational level that is in the bottom of the band. ....  | 29 |
| Figure 2.3: Normalized absorption and fluorescence for Rhodamine B molecule in ethanol solution.....   | 30 |
| Figure 2.4: Light trajectory undergoing amplification and multiple scattering and resultant incoherent random laser emission spectrum.....   | 33 |
| Figure 2.5: Example of light path forming a loop inside the gain medium and typical emission spectra presenting spikes. ....   | 34 |
| Figure 2.6: Example of scatter diagram with values of correlation coefficient. ....  | 38 |
| Figure 3.1: Schematic view of the experimental setup for random laser characterization for the Rhodamine 6G-doped silica xerogel matrix. ....  | 42 |
| Figure 3.2: Schematic view of the pumping direction and density of nanoparticles. Both sides will be analyzed and the emission will be captured always in the transmission. ....   | 42 |
| Figure 3.3: Schematic view of the experimental setup for random laser characterization for the Rhodamine 6G-doped PMMA fiber network. ....   | 43 |
| Figure 3.4: Example of extraction of the points to calculate C. (a) First spectrum with two highlighted wavelengths. (c) Pair of intensities from (a) placed in the intensity axis. (b) and (d) are the same procedure as (a) and (c). (e) shows the total points for calculating C. ....  | 45 |
| Figure 3.5: Schematic view of the steps the LabView routine performs to obtain the C values for every pair of wavelength in the spectra. ....  | 45 |
| Figure 3.6: Schematic diagram from getting the emission spectra to produce the 2D correlation map. Maps, emissions and values are merely illustrative. ....  | 46 |
| Figure 3.7: Schematic view of a scanning electron microscopy (SEM) apparatus. ....   | 47 |
| Figure 3.8: Schematic view of the main components of AFM. Inset is a real side view of a cantilever and the tip. ....  | 49 |
| Figure 4.1: Flow chart of the processes to Rhodamine 6G-doped xerogel preparation.....   | 52 |
| Figure 4.2: Optical microscopy of SF (a) and RF (b) of the lower concentrated sample and SF (c) and RF (d) of the higher concentrated sample. Atomic force microscopy of the higher (e) and lower (f) concentrated sample rough faces (left) and respectively profiles lines (right). (g) TiO <sub>2</sub> nanoparticles size distribution. ....   | 54 |
| Figure 4.3: (a) FWHM (blue circles) and integrated intensity emission (black squares) and (b) the spectral evolution with increasing pump energies for Rh6G-doped xerogel without TiO <sub>2</sub> scatters. ....  | 55 |
| Figure 4.4: (a) FWHM (blue circles) and integrated intensity emission (black squares) and (b) the spectral evolution with increasing pump energies for lower TiO <sub>2</sub> concentration Rh6G-doped xerogel when pumping from the RF. (c) FWHM (blue circles) and integrated intensity emission (black squares) and (d) the spectral evolution with increasing pump energies for lower TiO <sub>2</sub> concentration Rh6G-doped xerogel when pumping from the SF. .... | 56 |

|   |    |
|---|----|
| Figure 4.5: (a) FWHM (blue circles) and integrated intensity emission (black squares), (b) spectral evolution with increasing pump energies for higher TiO <sub>2</sub> concentration Rh6G-doped xerogel when pumping from the RF. (c) FWHM (blue circles) and integrated intensity emission (black squares), (d) spectral evolution with increasing pump energies for higher TiO <sub>2</sub> concentration Rh6G-doped xerogel when pumping from the SF, spikes are observed. .... | 57 |
| Figure 4.6: Schematic view of the absorption, scattering and emission processes for the case of pumping in the smooth face. ....  | 59 |
| Figure 4.7: Schematic view of the absorption, scattering and emission processes for the case of pumping in the rough face.....  | 59 |
| Figure 5.1: Schematic diagram of a typical electrospinning apparatus setup. ....  | 63 |
| Figure 5.2: MEV image of the 5% (m/m) Rhodamine B-doped PMMA nanofiber.....   | 64 |
| Figure 5.3: Emission spectra from different regions of excitation in the sample. The pump energy and spot area are fixed. Coherent and incoherent emission are acquired. ....   | 66 |
| Figure 5.4: (a) Emission spectra of the Rhodamine B-doped fiber for increasing pump energy. (b) Integrated intensity of the emission for increasing pump energy, a laser threshold is reached about 1μJ/pulse. ....   | 66 |
| Figure 5.5: Emission spectra of the first five pump pulses and the emission spectra of the pump pulse number 500. A long time excitation caused a subnanometer difference in the emission. ....   | 67 |
| Figure 5.6: Correlation map for an incoherent (a) and coherent (b) emission by pumping the sample in two different. On top of each map, the spectrally correspondent emission spectra for a pump shot. ....   | 68 |
| Figure 5.7: (a) Pearson correlation map for the coherent emission from each 100 shots taken in 500 shots evidencing the mode competition as a function of time. ....  | 70 |
| Figure 5.8: Pearson correlation map for an incoherent laser emission from each 100 shots taken in 500 shots total. A clear line widening dynamics is observed. ....   | 71 |
| Figure 5.9: (a) Spectral comparison of the first and last three emissions in the first 200 shots and (b) spectral comparison of the first and last three emissions in the 500 shots taken showing the subnanometer line widening of the emission.....   | 72 |
| Figure 5.10: (a) Incoherent random laser emission spectra and (b) integrated intensity and FWHM as a function of the pumping energy. Threshold is observed around 2.5 μJ/pulse.....   | 73 |
| Figure 5.11: Pearson correlation map of the first 100 shots (a). The area highlighted by the square is a negative correlation region between wavelengths marked amid the dashed lines. The first and last emission spectra of the set of spectra considered (b). The gray areas are the dashed lines correspondent in the emission spectra. ....  | 74 |
| Figure 5.12: (a) Pearson correlation map of 500 shots. The area highlighted by the solid lines informs that a blue shift occurs. (b) The first and last emission spectra of a total of 500 shots. The grey regions are the same wavelength regions bounded by the dashed lines.....   | 75 |
| Figure 5.13: Pearson correlation map for an incoherent random laser emission from each 100 shots taken in 500 shots total. ....   | 76 |

## LIST OF TABLES

Table 1: Energy threshold of the measurements performed as a function of scatter concentration in the sample. 58



## Content

|          |   |    |
|----------|---|----|
| <b>1</b> | <b>INTRODUCTION</b> .....   | 23 |
| 1.1      | Objectives .....  | 25 |
| 1.2      | Organization of the thesis .....  | 25 |
| <b>2</b> | <b>THEORETICAL BASIS</b> .....  | 27 |
| 2.1      | Basic concepts of laser .....   | 27 |
| 2.1.1    | Laser dyes .....  | 29 |
| 2.2      | Random Laser .....  | 30 |
| 2.2.1    | Incoherent Random Laser .....   | 32 |
| 2.2.2    | Coherent Random Laser .....   | 33 |
| 2.2.3    | Multiple scattering and light transport .....   | 36 |
| 2.3      | Pearson correlation coefficient .....   | 37 |
| <b>3</b> | <b>EXPERIMENTAL PROCEDURES</b> .....  | 41 |
| 3.1      | Rhodamine 6G-doped xerogel containing TiO <sub>2</sub> .....  | 41 |
| 3.2      | Rhodamine B-doped PMMA fiber network .....  | 43 |
| 3.3      | Scanning Electron Microscopy (SEM) .....  | 47 |
| 3.4      | Atomic Force Microscopy (AFM) .....   | 48 |
| <b>4</b> | <b>DECREASING LASER ENERGY THRESHOLD BY VOLUMETRIC SCATTERING DISTRIBUTION ENGINEERING</b> .....        | 50 |
| 4.1      | Introduction .....  | 51 |
| 4.2      | Materials and Methods .....   | 52 |
| 4.3      | Results and Discussion .....  | 53 |
| 4.4      | Conclusion .....  | 60 |
| <b>5</b> | <b>FLEXIBLE POLYMERIC FIBER RANDOM LASER AS POTENTIAL THERMAL AND CHEMICAL SENSOR APPLICATION</b> ..... | 62 |

|                        |                                   |           |
|------------------------|-----------------------------------|-----------|
| 5.1                    | Introduction .....                | 62        |
| 5.2                    | Materials and Methods .....       | 64        |
| 5.3                    | Results and discussions .....     | 65        |
| 5.4                    | Conclusions and perspectives..... | 76        |
| <b>REFERENCES.....</b> |                                   | <b>79</b> |

# 1 INTRODUCTION

*Laser* is the english acronym for *Light Amplification of Stimulated Emission of Radiation*. The pioneer work that experimentally showed laser action was published in 1960 by Maiman<sup>1</sup> which utilized a synthetic ruby crystal emitting in 694.3 nm. Since then, there have been a wide search for new structures and gain medium to laser construction, as rare-earth doped crystals (Nd:YAG), organic dyes (Rhodamine, Coumarin)<sup>2</sup>, gases (HeNe, CO<sub>2</sub>)<sup>3</sup>, fiber lasers<sup>4</sup>, random laser<sup>5</sup> etc.<sup>6</sup>. Parallel, the field of laser applications have been developed in different areas such as medical procedures<sup>7</sup>, holography<sup>8</sup>, communication<sup>9</sup> and also the large utilization of lasers to characterization of photophysical properties of new materials such as thin films, organic molecules, glasses, crystal and others.

The typical laser is formed by three main interacting elements: the excitation source, the gain medium and the optical cavity. The pump or excitation source is responsible for excite the atoms or molecules that compose the gain medium. The gain medium is positioned between a 100% reflective mirror and a partially reflective one, resulting the optical cavity. Excited atoms or molecules of the gain medium tend to spontaneously decay to the ground state emitting a photon in a random direction. A portion of those photons are reflected in the 100% mirror and get back to the laser medium and each one stimulates the decay of an atom or molecule, emitting a second photon with the same direction, wavelength, phase and polarization of the photon that caused the decay. This cascade effect of stimulated emission decay results a laser beam in the transmission of the partially reflected mirror<sup>10</sup>.

Dye laser is a class of laser that uses organic dyes as gain medium, usually in solution or working as the dopant of many solid state structures. Organic dyes are organic molecules with high emission quantum efficiency, that is, by shining light compatible with the molecule absorption band, it will absorb the light and, after a certain amount of time, it will emit it in a larger wavelength lying inside the fluorescence emission band. Organic dyes show a large emission band when compared to gases or rare-earth ions, therefore, they are great candidates to tunable laser with dozens of nanometers tunability<sup>11</sup>. Besides, due to the high variety of dyes and the fact that their molecular structure differences leads to different wavelength emission, results in a class of laser materials presenting emission in all the visible and near IR of the electromagnetic spectrum.

Among the vast number of laser classes, there is a special one called Random Laser. In this type of laser, the stimulated emission process is not activated by the mirrors in the optical cavity but by multiple scattering of light, in a way that the mirrors are replaced by scatterers in the volume of the gain medium or even externally to it. However, the mirrors in a typical cavity fix a direction of emission, while in random lasers, the emission can, in principal, be observed in all directions once the photon path inside the sample and the following output is random. The pioneering work that make the random laser possible was idealized just eight years after Maiman's paper and it presented a theoretical assumption of light generation with laser features by scattering particles as amplification mechanism and assuming a photon diffusion regime<sup>12</sup>. Only in 1994, there was an experimental validation of the random laser using TiO<sub>2</sub> nanoparticles in an ethanoic solution of Rhodamine 640<sup>13</sup>. Since then, many materials and architectures have allowed the scattering negative absorption mechanism proposed by Letokhov *et. al.*, including semiconductors<sup>14</sup>, optical fibers<sup>15</sup>, photonic crystals<sup>16</sup>, polymeric matrixes<sup>17</sup>, sol-gel materials<sup>18</sup>, rare-earth doped nanometric powders<sup>19</sup>, polymeric microstructures<sup>20</sup>, among others. Random laser materials gave rise to important applications, such as, imaging<sup>21</sup>, photonic chip<sup>22</sup>, dopamine sensor<sup>23</sup> and even medical applications which the random laser emission is used to differentiate cancerous and health human tissues<sup>24</sup>.

Due to the random laser property of lasing without external mirrors, it made miniaturized materials with laser-like emission characteristics possible. This fact opens a clear way to integrate lasers in portable devices such as lab-on-chip technology or even in sensors that can be taken to remote places or reach hostile environment. With this in mind, a goal for random laser material architecture is their fabrication with extremely low cost and practically disposable. Other issues concerning random lasing had some alternatives already presented in the literature such as beam directionality<sup>25</sup>, low laser energy threshold<sup>26-28</sup> and ease of manufacturing<sup>29</sup>.

Looking for those characteristics, in this work, we demonstrate two different random laser systems using methods of fabrication and materials that are among the cheapest ways in doing so. A vitreous matrix using one of the standard and simplest forms of silica xerogel fabrication via sol-gel process and a polymeric nanofiber using polymethylmethacrylate (PMMA) and obtaining the fiber via electrospinning technique. In addition, both structures are doped with Rhodamine molecules, which are one of the most common dye available.

## 1.1 Objectives

Overall, the objective of this thesis is to study the random laser properties of two classes of organic dye doped materials: a sol-gel based vitreous matrix and a polymeric fiber network. The former is a Rhodamine 6G-doped vitreous matrix fabricated via sol-gel process with inhomogeneously distributed TiO<sub>2</sub> nanoparticles in order to understand the mechanism of the random laser threshold by means of an inhomogeneous distribution of scatterers in the direction of the excitation axis and pumping both sides, one at a time. The latter was a Rhodamine B-doped network fiber in which a statistical method was applied in the emission spectra in order to understand random laser properties of this system and to propose a type of sensor based on the time evolution of the statistical properties.

The fundamental research on those materials was to characterize them as random laser hosts by means of laser threshold, emission linewidth and feedback mechanisms. However, beyond that, both class of materials presented features that allowed a deeper understanding of the random laser dynamics and applications. For the vitreous matrix with inhomogeneously scatterers distribution, we were concerning with answering: how would the energy threshold behave if the pumping light and amplification process, instead of experiencing a homogeneous distribution of scattering particles, encounter an increasing density of scatterers, or a decreasing one? In the case of the polymeric fiber material, based on the random laser emission features, our goal was to propose a new way of keeping track of sample degradation and laser mode competition as a function of time by applying statistical methods on the emission spectra.

## 1.2 Organization of the thesis

The further chapters of this thesis are organized as follows: in Chapter 2, we present the fundamental concepts of a laser, an overview on the physics of random laser from incoherent to coherent one and its respective theoretical explanations. A brief overview on Mie scattering properties and light transport in random medium is discussed. Finally, it is given an explanation on the Pearson correlation coefficient and how it was introduced in the emission spectra data treatment. In Chapter 3, we describe the experimental setup used to characterize the random laser emission on both systems studied and the LabView program to create the 2D map of correlation coefficients  $C$ . Also, a picture of the LabView block diagram and the front end of the program in question is shown in Appendix A.

The two following chapters present the results of this thesis. The introduction, materials and methods and results of each study are presented in two separated chapters. Chapter 4 encompasses the investigation of laser threshold for the Rhodamine 6G-doped silica xerogel matrix containing TiO<sub>2</sub> nanoparticles inhomogeneously distributed. We found that the way the pump beam encounters the nanoparticles distributed inside the sample can turn the threshold higher or lower compared to an undoped sample.

Chapter 5 displays the investigation of random laser emission on Rhodamine B-doped PMMA fiber network fabricated via electrospinning technique. The samples were provided by the Nanotechnology National Laboratory for Agriculture at *Embrapa Instrumentação* in São Carlos, SP. We describe the mode-locking transition from coherent to incoherent random laser just by changing the region of the sample we are exciting, exploiting the randomness of the fiber network due to the deposition technique. Also, we propose a new sensor using a method of time dynamic of the statistical approach to probe the line widening or mode competition of the emitted random laser.

## 2 THEORETICAL BASIS

### 2.1 Basic concepts of laser

The first step to understand the fundamental concepts of laser theory is the Planck's quantization of energy that successfully described the blackbody radiation. It states that energy is emitted or absorbed only in integral multiples of a small unit of energy, the quantum, which is proportional to the frequency of the radiation. Using the quantum hypothesis, Einstein focused the attention on atoms in cavity walls that were responsible for the generation of electromagnetic energy inside the cavity, and identified three processes that affect the number of atoms in the ground and excited energy states.

By assuming that the energy came in discrete packages as  $E = h\nu$  and the presence of two energy states, the three radiative processes, depicted in Figure 2.1 are as follows:

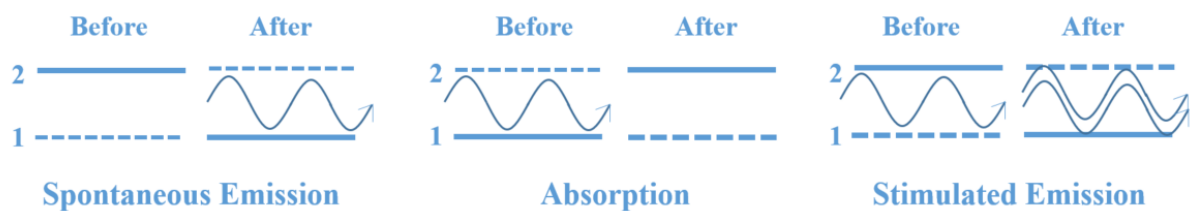


Figure 2.1: Diagram representing energy levels transitions such as spontaneous emission, absorption and stimulated emission.

**Source:** By the author.

**Spontaneous emission.** Atoms in state 2 decay spontaneously to state 1 releasing a photon which will be added to the cavity field.

**Absorption.** An atom in state 1 absorbs a photon from the field and is excited, happening to occupy the state 2.

**Stimulated emission.** Called the reverse absorption, an excited atom at state 2 is brought to the state 1 by a photon emission stimulated by a photon of the field. The emitted photon is added coherently to the field, with same frequency, phase, polarization and propagation direction as the photon that induced the atom to undergo the transition.

Considering  $N_1$  and  $N_2$  the number of atoms, respectively, in the ground state and in the excited state levels, the population distribution in the thermodynamic equilibrium is given by the Boltzmann law, as:

$$\frac{N_2}{N_1} = e^{-(E_2 - E_1)/kT} \quad (2.1)$$

in which  $k$  is the Boltzmann constant and  $T$  is the system temperature. In this way,  $N_1$  is always large than  $N_2$  because the right-hand side of the equation will always be less than one since  $E_2 > E_1$ , meaning that, in the equilibrium, there is no population inversion and, therefore, no light amplification. In other words, the total stimulated transition rate in the equilibrium is always absorptive or attenuating rather than amplifying. To be in a case of laser amplification, a pumping process must be added to the system, putting more atoms into the upper level and creating a population inversion<sup>30</sup>.

Besides amplification, a laser takes advantage of an optical cavity to provide feedback of the laser light and reach steady-state oscillations, which requires that the net gain have to be exactly equal the net loss in a way that a light round-trip in the oscillator neither grows nor decay in intensity. One of the most used optical cavity is the Fabry-Perrot resonator, made of two parallel mirrors promoting longitudinal steady-state waves. Therefore, for a total round trip in an optical cavity with a gain medium of length  $l_g$  placed between the mirrors of reflectivity  $R_1$  (100% reflective) and  $R_2$  (partly reflective to work as the laser output), considering only mirror losses, the gain coefficient  $\gamma_0$  must be sufficiently large in a way that

$$R_1 R_2 e^{2\gamma_0 l_g} \geq 1 \quad (2.2)$$

once the gain is exponentially increased for each round trip and light passes two times in the gain medium. We can rewrite this expression as

$$\gamma_0 \geq \frac{1}{2l_g} \ln \frac{1}{R_1 R_2} = \alpha \quad (2.3)$$

Defining  $\alpha$  as the total loss, we get to the statement that gain must be at least equal to the total loss of the cavity. We call the laser threshold the pump energy necessary to reach this condition, an important parameter to characterize the laser system<sup>31</sup>.

After all the considerations of laser conditions done so far, it is counter intuitive to think that adding scattering elements on this system would allow laser emission, once scattering would be a large loss factor. In fact, in conventional lasers this is the case. Nevertheless, for random lasers, the optical cavity is replaced for highly scattering elements internal or external to the gain medium in a way that the light scatters so many times that it has sufficiently time in the amplification volume to fulfill the gain be larger than the losses condition. This process will be extensively explained in the next sections.

### 2.1.1 Laser dyes

Dye lasers were first experimentally verified in 1966, when several other laser active materials had already been found. They have some attractive aspects, for instance, they can be easily tunable over a wide range of wavelengths due to the large emission band. Dyes can be used in solid, liquid and gas phases with controlled concentrations. The cost of such molecules are very small, compared to active medium of solid-state lasers. They exhibit very high gain due to the large emission and absorption cross sections and large fluorescence quantum yields<sup>2,11,32</sup>. So, they are very good candidates to be used as random laser active medium, since they can be pumped efficiently and would support the low cost philosophy of the random laser devices studied on this work.

The fact that dyes have large emission and absorption bands make them a four-level laser system, as represented in the schematic energy levels in Figure 2.2. The presence of only two bands could lead to a misconception that we are dealing with a two level system, which cannot produce population inversion once the absorption frequency is the same as the emission, and therefore, the pumping light both excites via absorption and depopulate the excited state via stimulated emission, thus, the saturation limits the inversion to 50%. The four-level system in those molecules are due to the different decay rates of the lower and higher state of each band ( $S_0$  and  $S_1$ )<sup>33</sup>.

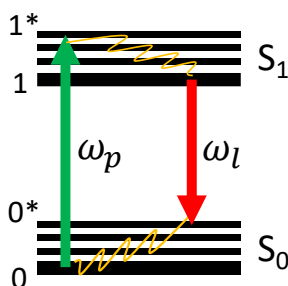


Figure 2.2: Schematic energy levels of an organic dye. The ground and excited states have several vibrational states. The molecule quickly relaxes to a vibrational level that is in the bottom of the band.

**Source:** By the author.

The pumping source excites the dye molecule by promoting it from the ground state 0 to the higher vibrational energy state 1\* that non-radiatively decays quickly into state 1. The molecule emits a photon with frequency that is relative to the radiative decay from 1 to 0\* and, finally, a quickly non-radiative decay from 0\* to 0 level returns the molecule to its initial vibrational ground state. Once the non-radiative transition occurs in  $\sim 0.1$  ps, nearly all molecules are either in level 0 or in level 1. Therefore, the absorption and emission frequencies are decoupled and the population inversion feasible.

We can see in the absorption and emission spectra of the Rhodamine B molecule showed in Figure 2.3 that the intensity maximum of the bands are separated in wavelength (frequency), which leads to a four-level system for the molecule. In addition, the linewidth of both bands is large (almost a hundred of nm), which encompasses almost all the visible range of the electromagnetic spectrum. For example, the laser emission could be tuned in the fluorescence band from 560 nm to more than 600 nm.

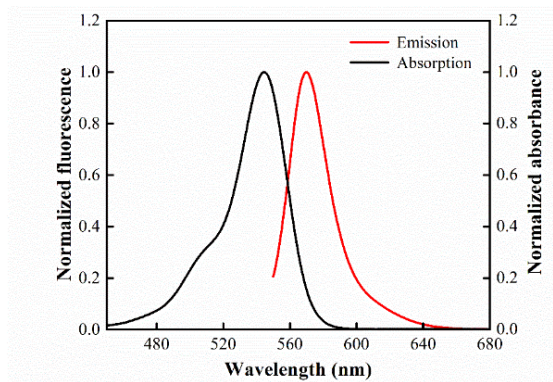


Figure 2.3: Normalized absorption and fluorescence for Rhodamine B molecule in ethanol solution.

**Source:** By the author.

For random laser systems, the large range of the emission band also contributes to the possibility of a large number of modes in the laser emission. Once the emitted photons are of great range of frequency, it can result in modes of wavelengths with various nanometers of separation between them. For the Rhodamine B-doped PMMA nanofiber random laser demonstrated in this work, it can support laser emission with peaks distancing 20 nm from each other.

## 2.2 Random Laser

A random laser concerns a class of lasers that takes advantage on multiple scattering of photons to promote light amplification in systems without well-defined cavity modes of standard lasing structures<sup>34</sup>. Yet this system is not bounded by any mirrors, it presents characteristics that are similar to those of conventional lasers. For instance, lasing in any of these systems requires optical amplification and feedback. The former is achieved by an excited gain medium that is stimulated by incoming photons to emit. The latter is quite different from conventional lasers to random lasers. In ordinary lasers, the presence of an optical cavity sets

up a defined phase relation of waves propagating in opposite direction and, consequently, defines the possible cavity modes. In random lasers, the first hypothesis of lasing in these systems was proposed as a propagation of photons described by a diffusion equation, which can have laser emission characteristics such as threshold, spectral narrowing, relaxation oscillations etc., yet this diffusion treatment ignores the wave nature of light and have no phase information.

The light diffusion phenomenon occurs due to an increase in path length that light travels inside an amplifying volume caused by multiple scattering, that is, light is forced to change its propagation direction due to random nanostructures embedded in the medium volume in a way that would result in a long time to reach free space. There are three different models to explain light scattering by particles depending on the relative size of them. The Rayleigh model, which refers to a scatterer that is smaller than the wavelength scattered. When the scatterers are of the order of the wavelength, the Mie scattering model is more accurate for this relative size range, but the theory is based on solving the Maxwell's equations with appropriated boundary conditions, which is pretty extensive. A Feynman's handwaving argument states that the  $N$  microscopic dipoles that makes up a scatterer radiate in phase if they are within half a wavelength of each other resulting constructive interference. Therefore, scattering in this regime can be very strong with large scattering cross section<sup>35,36</sup>.

The photonic field of random laser opens a path both in theoretical and experimental studies. The discovery of such kind of laser provided a wide search for materials that could support this laser type and the applications were from sensors to microfluidics, optical to medical devices. From the theoretical perspective, random laser systems have been challenging scientists once the randomness of the system must be put together with the laser theory equations. In this framework, there is a spectrum of different theories and approaches to accomplish it. It is interesting to note that experiment and theory walk together in this field. New discoveries in sample characteristics and emission leads to different ways of theatrically modelling the random laser system. The spectrum of theories can be summarized by analyzing a specific feature of those systems: the type of feedback presented in the random laser, incoherent or coherent feedback. It is by this perspective that the following subsections are organized.

### 2.2.1 Incoherent Random Laser

What happens if instead of a mirror to provide feedback and return the photons back to the gain medium, one uses a scattering surface? Ambartsumyan et. al.<sup>37</sup>, replacing one mirror of the Fabry-Perot cavity with a scattering surface, first realized it. In this case, light of the cavity returns to the gain medium experimenting multiple scattering, changing its direction every time it is scattered. For this reason, there is no spatial resonances of the electromagnetic field and the cavity tends to be continuous, that is, it does not contain discrete components of resonant frequencies. The only resonance element in this kind of laser is the atom or molecule transition line of the active medium. In fact, this is exactly what was observed, i.e., instead of equally spaced high-Q resonances, there appeared a large number of spectrally overlapped resonances of low-Q forming a continuous spectrum. This is what occurs in the incoherent random laser or non-resonant feedback random laser.

Instead of a scattering surface, Letokhov<sup>12</sup> developed a theory where the active medium itself was filled with scattering centers. He realized that when the photon mean free path is much smaller than the dimensions of the scattering medium but much longer than the photon wavelength, the motion of it is diffusive, so he solved the diffusion equation and included the gain by simply reversing the sign of the usual loss term. The diffusion equation for the photon energy density is as follows:

$$\frac{\partial W(\vec{r}, t)}{\partial t} = D \nabla^2 W(\vec{r}, t) + \frac{v}{l_g} W(\vec{r}, t) \quad (2.4)$$

$v$  is the transport velocity of light inside the scattering medium,  $l_g$  is the gain length and  $D$  is the diffusion constant given by:

$$D = \frac{v l_t}{3} \quad (2.5)$$

$l_t$  is the transport mean free path. The general solution to the diffusion equation can be written as:

$$W(\vec{r}, t) = \sum_n a_n \Psi_n(\vec{r}) e^{-(DB_n^2 - v/l_g)t} \quad (2.6)$$

$\Psi_n(\vec{r})$  and  $B_n$  are, respectively, the eigenfunctions and eigenvalues of the problem with boundary conditions  $\Psi_n = 0$  at the boundary of the random medium. The solution of  $W(\vec{r}, t)$  changes from an exponential decay to an exponential growth in time when crossing the threshold

$$DB_1^2 = \frac{v}{l_g} \quad (2.7)$$

$B_1$  is the lowest eigenvalue. In fact, the intensity will not diverge because gain depletion will make  $l_g$  increases. Intuitively, we can derive that the length a photon travels in the scattering medium before escaping must be larger or equal than the average length a photon travels before generating a second photon by stimulated emission<sup>38</sup>. Only 26 years later the Letokhov's predictions, his theory was experimentally confirmed.

A way to visualize it is to look at the photon path in an active medium containing scattering particles that are randomly distributed in the medium volume, as depicted in Figure 2.4. By pumping it, some excited molecules will spontaneously emit a photon somewhere in the sample volume. In its path inside the sample, it will stimulate other excited molecules to emit, so those photons will travel in the same direction with the same phase and frequency. Additionally, those photons will undergo several scattering process before reaching the free space. The fact that the mean free path of the photons is much smaller than the sample's length make the resultant emission takes laser-like properties.

In the case of the incoherent random laser, the emission spectrum profile is a gaussian-like curve with nanometer or even subnanometer linewidth. The single peak emission characteristic of this type of random laser comes from the fact that once there is no resonant feature, the only remaining resonant element is the molecular transition.

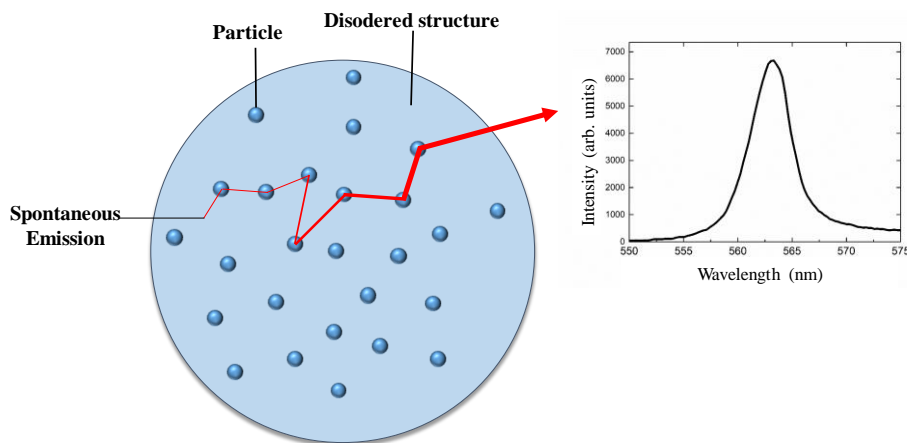


Figure 2.4: Light trajectory undergoing amplification and multiple scattering and resultant incoherent random laser emission spectrum.

Source: By the author.

## 2.2.2 Coherent Random Laser

Introducing a higher density of scattering particles in the sample, it was observed a completely new phenomenon. In the random laser emission spectra, instead of a gaussian

emission profile as before, multiple emission lines appeared in the spectrum<sup>39,40</sup>. The new peaks present much narrower linewidth compared to the incoherent random laser and by increasing the pumping energy, the number of peaks emitting increases. The first attempt to explain it was that a transition from non-resonant to resonant feedback random laser emission occurred. Therefore, many ideas have been developed to give an explanation on how a laser without cavity would present resonant feedback.

Firstly, Cao *et. al.* proposed that the feedback is due to formation of closed loops in the photon trajectory. That is, when photons multiple scattered returns to a scatterer from which it was scattered before, the light path forms a closed trajectory. Once the trajectory length is the same for all photons in the loop, the interference of them is always constructive, so, when the amplification along the loop exceeds the loss, laser oscillation could occur in the loop, which serves as a laser resonator and it will represent a narrow discrete peak. An example of photon trajectory and emission spectrum is depicted in Figure 2.5. In Cao's work, the experimental demonstration of this phenomenon was achieved using aggregated powder of ZnO nanorods and ZnO/GaN nanoparticles. In those systems, the active particles work both as active medium and scatterers<sup>14</sup>. Later on, the coherent random laser was also found in Rhodamine 640 dissolved in ethanol containing ZnO particles<sup>41</sup>.

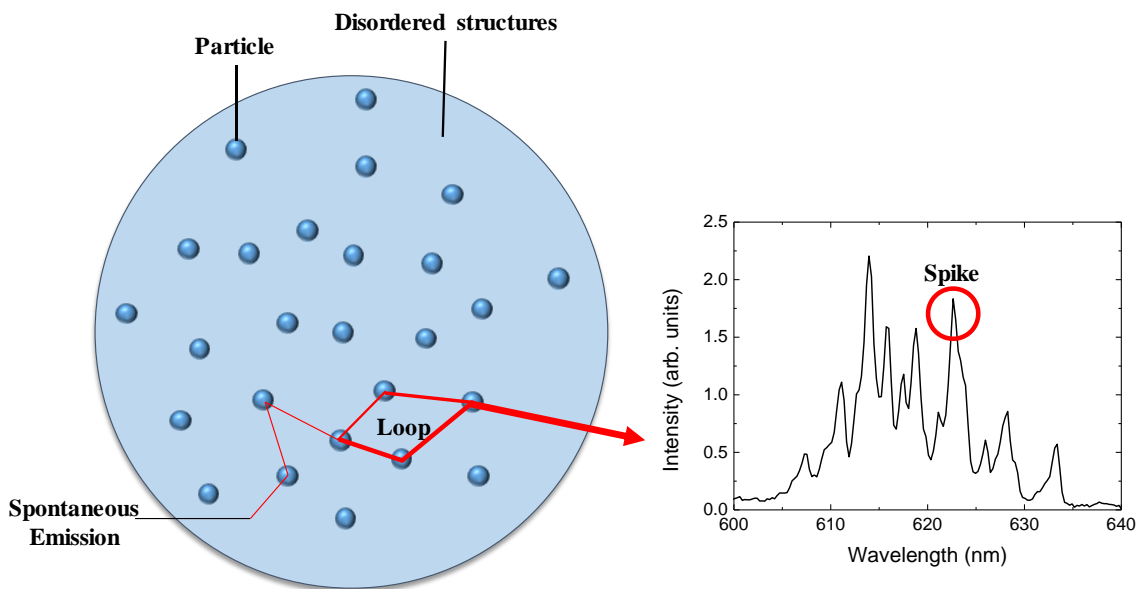


Figure 2.5: Example of light path forming a loop inside the gain medium and typical emission spectra presenting spikes.

**Source:** By the author.

Another approach to explain the formation of cavities was the Anderson localization of light. If the scattering mean free path  $l_s$  is of the order of the photon wavelength, light is scattered even before a complete oscillation of its electromagnetic field. Therefore, interference effects must be taken into account leading to a correction of the diffusion coefficient, which is now given by

$$D \approx D_0 \left[ 1 - \frac{1}{(kl_s)^2} \right] \quad (2.8)$$

where  $k = 2\pi/\lambda$  is the photon wave number and  $D_0$  is the uncorrected diffusion coefficient. The expression states the so called Ioffe-Regel criterium<sup>42</sup>, given by  $kl_s \sim 1$ , resulting  $D \sim 0$ , that is, the light diffusion ceases, and the light is called localized.

A large number of numerical studies was performed to simulate the Anderson localization in one-dimensional models<sup>43,44</sup> that provided explanation to some experimentally observed results such as mode repulsion and saturation of the number of lasing modes. In<sup>45</sup>, a 1D model of random laser showed that multilasing peaks are due to the interplay between localization and amplification. Localization makes the lasing mode strong around the localization center and exponentially small away from its center. When a mode lases, only the modes far enough from this mode can lase afterwards. So, each mode seems to repel each other. Once the random laser is a finite system, this effect of mode repulsion results in a saturation of the number of modes lasing. It is worth mentioning that it has never been convincingly demonstrated that light in strongly scattering three-dimensional samples was indeed at the Anderson localization state.

An alternative mechanism of formation of cavities that could be responsible for coherent feedback in random media was presented<sup>46</sup> and experimentally supported by lasing in  $\pi$ -conjugated polymers<sup>47,48</sup>. It states that the ring cavity model discussed before requires an extremely high gain to achieve the lasing threshold condition for a loop, since in each scattering, most of the energy gets scattered out of the loop. It was argued that the “impurity loops” are likely to generate a broad frequency spectrum rather than isolated resonances. Therefore, it was suggested that random fluctuations of the refractive index of a disordered medium could lead to large ring-like configuration allowing light trapping for enough time to serve as a resonator.

Instead of dealing with a ring-like resonator, another model of random laser was proposed where they were treated as lasers with distributed feedback. In contrast to the case of distributed feedback lasers, the feedback does not originate from a periodic structure, but from a random spatial variation of the refractive index, caused by scattering nanoparticles<sup>49,50</sup>.

Along with the effort to explain the discrete peaks emission in highly scattering systems, a new experimental phenomenon was observed: an emission spectrum containing very sharp spikes for very weakly scattering samples<sup>51,52</sup>. In recent paper<sup>51</sup>, it was performed a Monte Carlo simulation to model light random walk transport through the studied random media. The experimental and simulated emission spectra showed a weak correlation between the number of spikes in the spectra and the mean free path, that is, even for large value of mean free path, which means a weakly scattering system, there were spikes presented in the emission. Then, it was argued that each individual peak corresponds to a single spontaneous emission event that followed an extremely long light path through the sample and was consequently strongly amplified.

Trying to differentiate the spiky emission from system with weakly and strongly scattering processes, other publications<sup>53,54</sup> proposed that the “spikes” are presented in single-shot spectra of amplified spontaneous emission (ASE) and are intrinsically stochastic and vary from shot to shot even though the disorder is static. As mentioned before, those spikes are single spontaneous emission events that take long open paths inside the amplifying random medium. On the other hand, “peaks” are related to true lasing modes formed by randomly distributed feedback.

### 2.2.3 Multiple scattering and light transport

The Mie theory is constructed by solving the Maxwell’s equations with proper boundary conditions for spherical or cylindrical particles. The proportion between the incident light wavelength and the size of the particle to be considered in the Mie range is:

$$x = \frac{2\pi\eta a}{\lambda} \approx 1 \quad (2.9)$$

which  $a$  is the radius of the particle,  $\eta$  is the refractive index of the medium, and  $\lambda$  is the incident light wavelength. Besides the Mie scattering theory is far too extensive and have no shortcut, the real random laser systems present particles that are not perfectly sphere and consists of not only a single particle scattering process, but a multiple scattering one. An extensive treatment of the problem is given in references<sup>55–58</sup>.

In order to account all the possible processes taking place inside de highly scattering active medium, we can define quantities that express some average distances with respect to scattering and absorption. For example,  $\ell_s$  is called the scattering mean free path, the average distance between two scattering events, and  $\ell_a$  is the average distance between two absorption events, which depends on the respective scattering and absorption cross sections ( $\sigma_s$  and  $\sigma_a$ )

and the particle density  $n$  by  $\ell_s = \frac{1}{n\sigma_s}$  and  $\ell_a = \frac{1}{n\sigma_a}$ , quantifying how strongly the material influences the wave field by the scattering or absorption processes.

For a random laser system, we can have systems that  $\lambda \ll \ell_s \ll L$ ,  $L$  being the size of the system. It is for this system that we expect incoherent emission, because the scattering is weak. If  $\lambda \leq \ell_s$ , we are at a strongly scattering medium where the light/particle interaction happens in virtually one oscillation of the electromagnetic field of light, completely affecting the transport. In this regime, light interference must be taken into account and we can approach the Anderson localization of light as discussed in the coherent random laser emission that it could be a reason for the peaks presented in the emission spectrum of those systems.

Another interesting parameters are the gain length  $\ell_g$ , which is the average length the light intensity is amplified by a factor of  $e$ , and the amplification length  $\ell_{amp}$  is defined as distance mean square between the initial and final points of  $\ell_g$ . For example, in a homogeneous medium without scattering, light travels in a straight path, so  $\ell_{amp} = \ell_g$ . In a scattering medium,  $\ell_{amp}$  is related to the diffusion coefficient ( $D$ ) as  $\ell_{amp} = \sqrt{Dt}$ , in which  $t = \ell_g/v$ , and  $v$  is the light velocity in the medium.

## 2.3 Pearson correlation coefficient

In statistics, the Pearson correlation coefficient (PCC), or also referred as bivariate correlation or just Pearson's  $r$  is a measure of the linear correlation between two variables  $X$  and  $Y$ . The empirical and theoretical developments that defined regression and correlation as statistical topics were presented by Sir Francis Galton in 1885<sup>59</sup>. Ten years later, Karl Pearson published the Pearson's  $r$ , defined as the covariance of the two variables divided by the product of their standard deviations<sup>60</sup>. The value of the Pearson correlation can range from +1 to -1, where +1 is total positive correlation, 0 is no correlation at all and -1 is total negative correlation, some examples of diagrams with different correlations are showed in Figure 2.6. In other words, given a number  $N$  of pairs of two quantities, they are said correlated if the increasing or decreasing of one of the quantities implies an increase or decrease in the other one. Yet, if this implication is completely linear, they are said to be fully correlated. The PCC method found applications on imaging correlation of autonomous vehicle where the PCC are evaluated from the intensity of each pixel of a set of images<sup>61</sup>. Furthermore, PCC was already used in

agriculture science to find correlation between the petal length and width and which tree species these factor are correlated or not<sup>62</sup>.

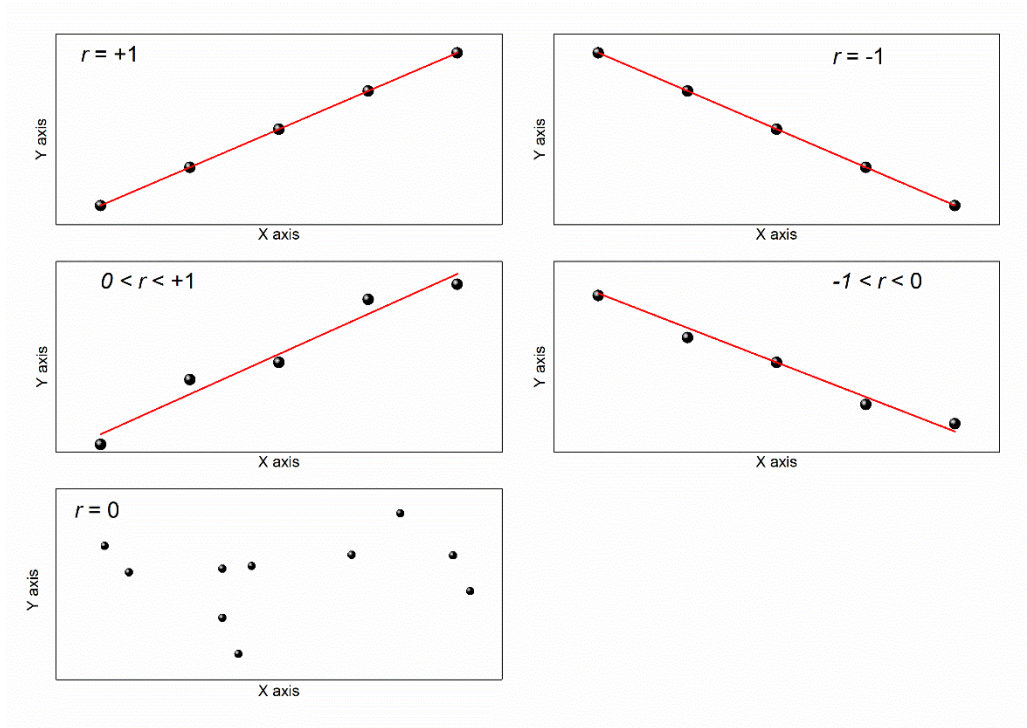


Figure 2.6: Example of scatter diagram with values of correlation coefficient.

**Source:** By the author.

The PCC is a dimensionless index invariant to linear transformations of either variable. The mathematical formula for this measure is as follows:

$$r = \frac{\sum(X_i - \bar{X})(Y_i - \bar{Y})}{[\sum(X_i - \bar{X})^2 \sum(Y_i - \bar{Y})^2]^{1/2}} \quad (2.9)$$

In the numerator, the *i*th values are centered by subtracting out the mean of each variable and the sum of the products of the centered variables are accumulated. The denominator adjusts the scales of the variables for *r* to be dimensionless and ranges from -1 to +1.

A few publications in the photonics area presents statistical approaches to obtain more complex information about the system. In the random laser field, the situation is the same. Exploiting the existed works in statistical approaches, one can find two papers that stands out. Both use the Pearson correlation coefficient as the statistical tool, which was motivation to use the mentioned tool in this thesis. The pioneer work, to the best of our knowledge, was the done

by M. Leonetti and co-workers<sup>63</sup>, which a PCC method was used together with the coupled mode theory to show the mode locking transition on random lasers. It was shown that a transition from coherent to incoherent emission also leads to a phase locking transition. This effect was related to the fact that the PCC values tends to increase when transitioning from coherent to incoherent emission. Another PCC application is found in the M. Montinaro and co-workers paper which showed a difference in the modes intensities correlation in fibers samples with and without TiO<sub>2</sub> nanoparticles doping. This was done by producing the PCC maps from both sample emissions.

The PCC formula specifically for a pair of intensities related to two wavelengths of a set of emission spectra is as follows:

$$c(\lambda_j, \lambda_k) = \frac{\sum_{i=1}^N [I_i(\lambda_j) - \bar{I}(\lambda_j)] [I_i(\lambda_k) - \bar{I}(\lambda_k)]}{\sqrt{\sum_{i=1}^N [I_i(\lambda_j) - \bar{I}(\lambda_j)]^2} \sqrt{\sum_{i=1}^N [I_i(\lambda_k) - \bar{I}(\lambda_k)]^2}} \quad (2.10)$$

in which, N is the number of spectra analyzed,  $I_i$  is the intensity of the  $i$ th spectrum at a certain considered wavelength ( $\lambda_j$  or  $\lambda_k$ ), and  $\bar{I}$  is the average intensity of the N spectra at one of the wavelengths considered. Some works have been using this strategy to obtain differences between modes in incoherent or coherent emissions. By selecting several pairs of wavelengths corresponding to two distinct modes, it is possible to perform the C coefficient calculation for each pair and when the average of C's gets the smaller value, the emission turns to be coherent. This became clearer when a C coefficient was calculated for every pair of wavelength available in the emission spectra. For example, for a spectrum with 100 wavelengths would produce a matrix of 10,000 values of C which can be visualized in a 2D heatmap. In this case, the principal diagonal will always be equal to 1 once the wavelength will always be fully correlated with itself. The main advantage in doing it is that there is no lack of information once by calculating C only for a few pairs of wavelength could lead to incomplete results and choice of wavelength that does not represent the actual correlation.

It is important to note that the points and respective lines in Figure 2.6 are graphic illustrations that only one value of C is calculated from it. Thus, in the case of a PCC in random laser emission spectra, the correspondent graph would have the x axis as the intensity of some wavelength  $\lambda_1$  and the y axis as the intensity of some wavelength  $\lambda_2$ . The points would be pairs of intensity given a fixed pair of wavelengths. This graph would lead to a value of C for this specific pair of wavelengths. The 2D map has its x and y axis as wavelength (instead of the intensity at that wavelength), in a way that a single pixel of the 2D correlation map is a value

of  $C$  for the corresponding pair of wavelengths that the pixel lies in the  $x$  and  $y$  axis. The  $C$  value is represented by the corresponding color in the color palette.

## 3 EXPERIMENTAL PROCEDURES

The setup for measuring the emission spectra of both set of samples used as excitation source a frequency-doubled (532 nm) Q-switched mode-locked Nd:YAG laser delivering a 100 ps pulse train. In order to set the excitation to single pulse operation, a Pockels cell with a crossed polarizer was added to the apparatus. The laser beam pass through both optical components in order to control the pump energy delivered to the sample. The laser beam was focused in the sample with a 5 cm focal length lens resulting in a beam waist of 150  $\mu\text{m}$ . The light emitted by the sample was acquired by a multimode optical fiber connected to a spectrometer (Ocean Optics HR4000). The apparatus described are the same for both set of samples, the detailed features of each measurement are presented in the next subsections.

### 3.1 Rhodamine 6G-doped xerogel containing $\text{TiO}_2$

The random laser characterization of the xerogels was performed by studying two spectral emission features: the emission intensity and full width at half maximum as a function of the excitation energy. The measurements were performed in both sides of each xerogel sample to investigate the effect of the inhomogeneous configuration of the scatter centers. Hence, the excitation beam is perpendicular to the sample surface and the optical fiber that capture the random laser emission is placed in behind the sample perpendicular to the other sample surface.

An important laser feature measured was the laser energy threshold defined as the excitation energy in which there is a change in the angular coefficient of a bilinear fit of the experimental data of emission intensity. The detailed schematic experimental setup for this set of measurements is depicted in Figure 3.1.

As already mentioned, the sample is inhomogeneously doped with nanoparticles. The scatterer density changes in the same direction as the pump beam penetrates in the sample. Thus, by exciting the sample from one side or another will result in two different absorption, emission and scattering processes. If the excitation takes place in the surface that is close to the more densified nanoparticles volume, the scattering events will be large and the absorption/emission process will be a completely different dynamic than exciting by the surface that presents relative low scatterer density. Consequently, this is exactly what we present in the

results section: given a xerogel sample, we excite at one surface at a time and get the respective energy threshold. The schematic view of how the nanoparticles are distributed in the sample and the pump direction that will be performed one at a time is depicted in Figure 3.2.

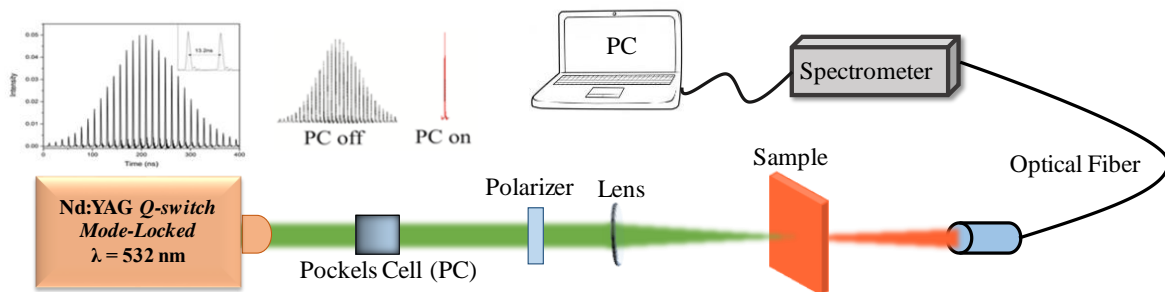


Figure 3.1: Schematic view of the experimental setup for random laser characterization for the Rhodamine 6G-doped silica xerogel matrix.

**Source:** By the author.

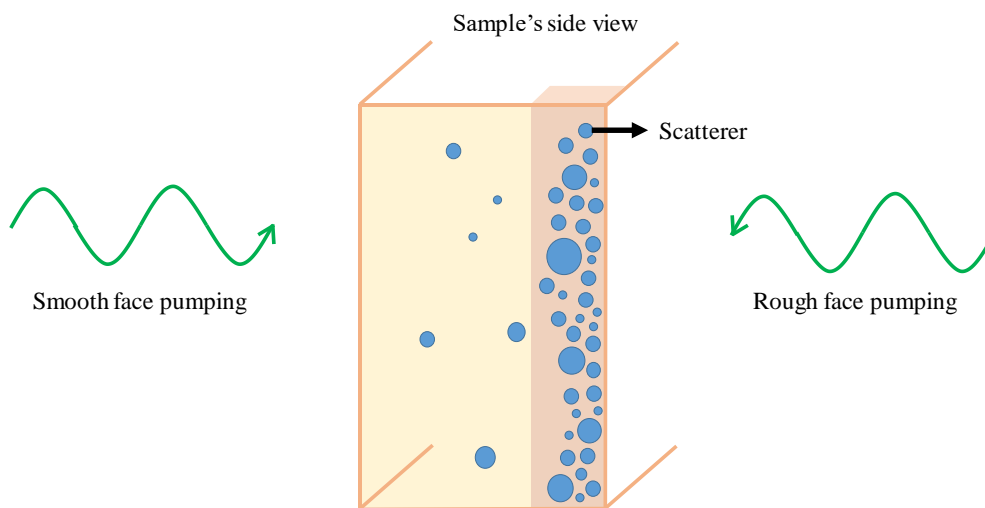


Figure 3.2: Schematic view of the pumping direction and density of nanoparticles. Both sides will be analyzed and the emission will be captured always in the transmission.

**Source:** By the author.

The diameter size distribution of the  $\text{TiO}_2$  nanoparticles were measured with the Zetasizer Nano via Dynamic Light Scattering (DLS) technique. The sample was prepared by dissolving 2 mg of powder  $\text{TiO}_2$  in 2 ml of ethanol. The resultant solution was homogenized in ultrasonic bath for 30 minutes. Following, it was diluted 10  $\mu\text{l}$  of the bathed solution in 1 ml of ethanol in order to obtain a sufficiently diluted solution to avoid particle aggregation. The final solution was placed in a cuvette and submitted to analyses.

## 3.2 Rhodamine B-doped PMMA fiber network

The experimental apparatus differentiates from the previous one just by the sample position and emission capturing. The sample is placed  $45^\circ$  from the beam perpendicular plane. The emission light is captured in the reflection by two lens (telescope) that focus and converges the light to a 1 mm core optical fiber. The detailed experimental setup is shown in Figure 3.3.

The fiber network random laser had its energy threshold characterized as well. In these samples, we performed the Pearson correlation that requires an emission spectrum acquired for each pump pulse. For example, if the laser is set to a repetition rate of 20 Hz, it will deliver a pulse each 50 ms to the sample, which will emit in the same rate. Therefore, we set the spectrometer software to capture a spectrum each 50 ms. Also, we can set the spectrometer to get a number N of saved spectra.

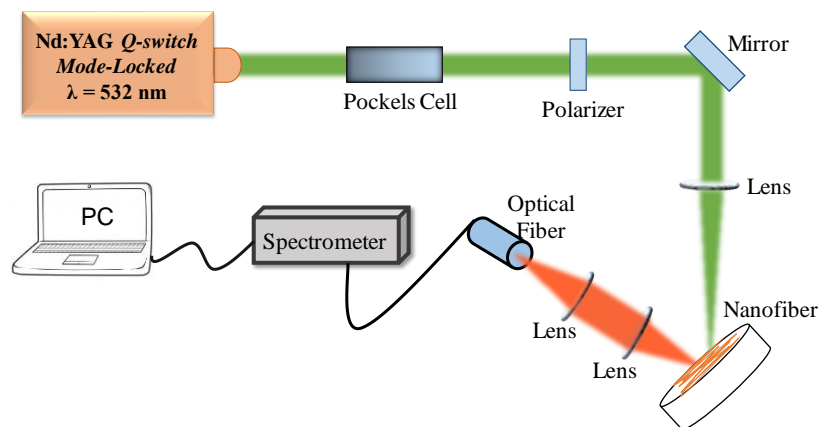


Figure 3.3: Schematic view of the experimental setup for random laser characterization for the Rhodamine 6G-doped PMMA fiber network.

**Source:** By the author

The calculation of the correlation coefficient  $C$  is done as follows: for a set of emission spectra, we begin with a pair of wavelengths within it and calculated  $C$  from that. The first step to calculate  $C$  is to take the emission intensities for those two wavelengths in the first emission spectrum of the set, as show in Figure 3.4a, then, we place them in a plot which the axis are the intensities of each wavelength considered, as shown in Figure 3.4c. The same procedure is done for the second emission spectrum, as shown in Figure 3.4b and Figure 3.4d. After repeating this procedure for all spectra in the set, it results in a graph, shown in Figure

3.4e, which is possible to calculate the C value for this specific pair of wavelengths just like the examples depicted in the Figure 2.6. The calculated value of C is then represented by a pixel in the heatmap corresponding the pair of wavelengths used to get the intensities. If we collect all the intensities corresponding to all the wavelengths in a single emission spectrum and save them in a row vector, the intensities of all the wavelength and all the spectra will result a matrix with the number of columns been the number of wavelengths and the number of rows been the number of spectra. So, to select a pair of wavelengths, we just choose two columns of the matrix. Thus, repeating the mentioned procedure to calculate C for other wavelengths is done just by selecting two different columns. The schematic view of the complete path from getting the emission spectra to produce the 2D correlation map are depicted in Figure 3.6. Each pair of wavelengths will result in a C value that is represented in a pixel in the correlation map. So, doing that for all possible pairs, we get the whole map.

The calculation of the C coefficients was performed in a LabView program completely developed by me, which reads the N emission spectra and select the desirable spectrum region, gets the intensity of all wavelength for each spectra, proceeds with the calculation of the average intensity of the N spectra for each wavelength and, finally, gets the normalized terms. Then, the intensities and the averaged ones enter a double for loop that for a given wavelength, calculates the C value with all the other wavelengths including itself. A square matrix is the output resultant C values, in which the number of rows and columns are equal to the number of wavelengths considered.

The fabrication of a series of consecutive maps was performed by placing the whole program in a for loop with the counter controlled by the number of shots that one wants in each correlation map. For instance, if we have  $N = 1000$  emission spectra and we want 100 spectra for each C map calculation, the for loop will cycle 10 times. The first cycle will result a map using the spectra 0 from 99 followed by a map calculated from the spectra number 100 to 199 and so on until the C map from 900 to 999. Each cycle will result a square matrix as discussed before and it is automatically saved in a .txt file in a folder chosen by the user. The correlation maps are shown in the front end of the program but we treat the square matrix in the Origin software which presents more data manipulation and analysis tools. A schematic view of the steps the LabView routine performs to get values of C for the 2D mapping is shown in Figure 3.5.

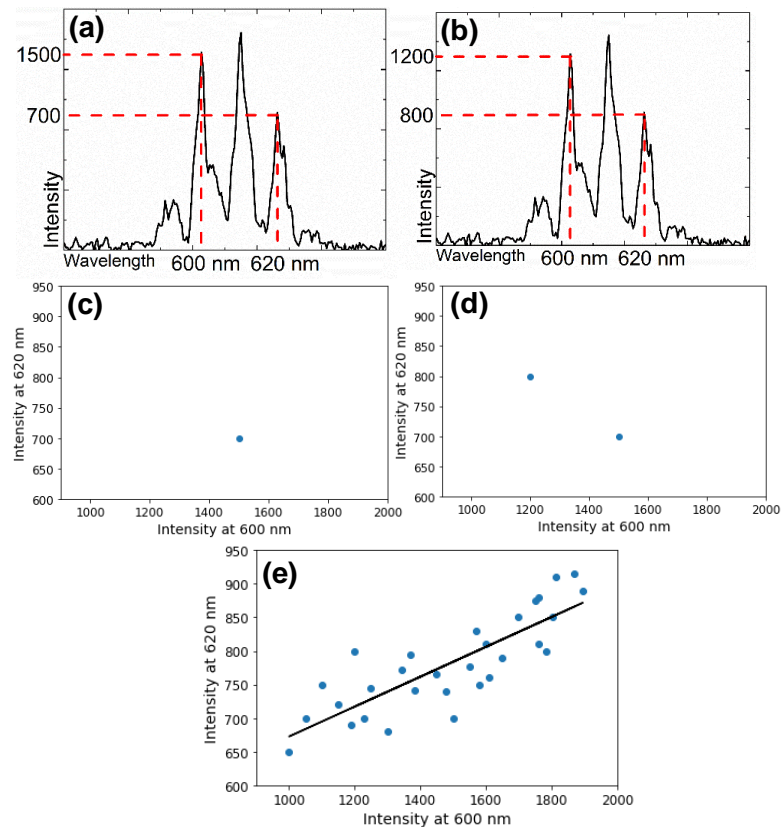


Figure 3.4: Example of extraction of the points to calculate C. (a) First spectrum with two highlighted wavelengths. (c) Pair of intensities from (a) placed in the intensity axis. (b) and (d) are the same procedure as (a) and (c). (e) shows the total points for calculating C.

Source: By the author.

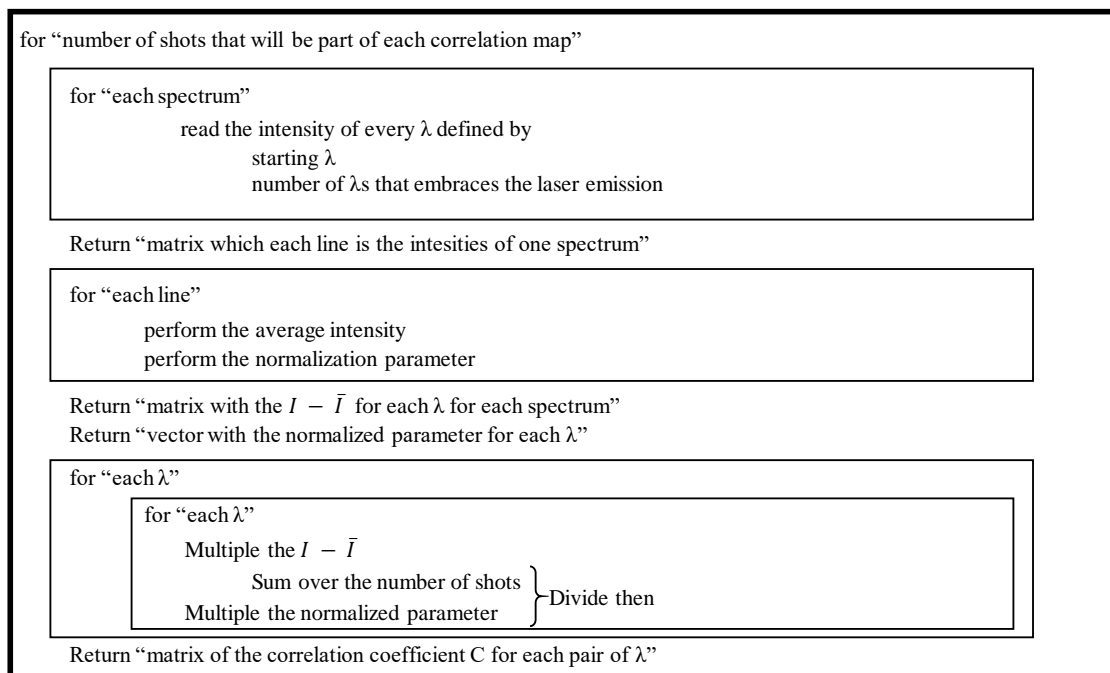


Figure 3.5: Schematic view of the steps the LabView routine performs to obtain the C values for every pair of wavelength in the spectra.

Source: By the author.

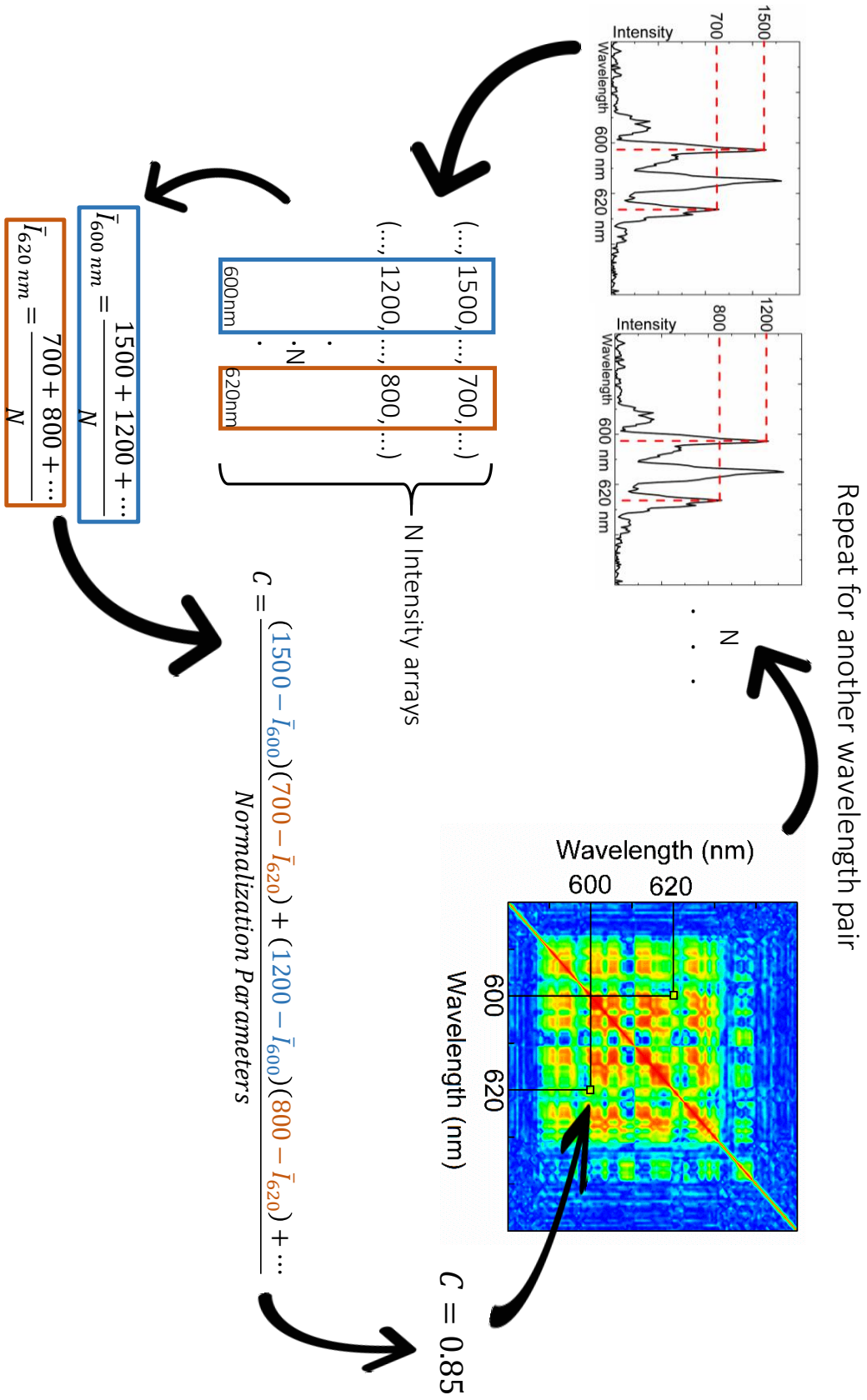


Figure 3.6: Schematic diagram from getting the emission spectra to produce the 2D correlation map. Maps, emissions and values are merely illustrative.

Source: By the author.

### 3.3 Scanning Electron Microscopy (SEM)

The scanning electron microscopy is a type of electron microscopy, which utilizes a focused beam of high-energy electrons to scan the sample surface producing an image. Those accelerated electrons reach the sample and are decelerated by the electron-atom interaction. A variety of signals results from the interaction, such as secondary electrons, backscattered electrons, diffracted backscattered electrons, X-ray and visible light photons and heat. Some of those signals reveals some properties of the sample. For example, the secondary electrons produce the SEM images, the diffracted backscattered electrons are used to determine crystal structures and orientations, the X-ray photons are used for elemental analysis.

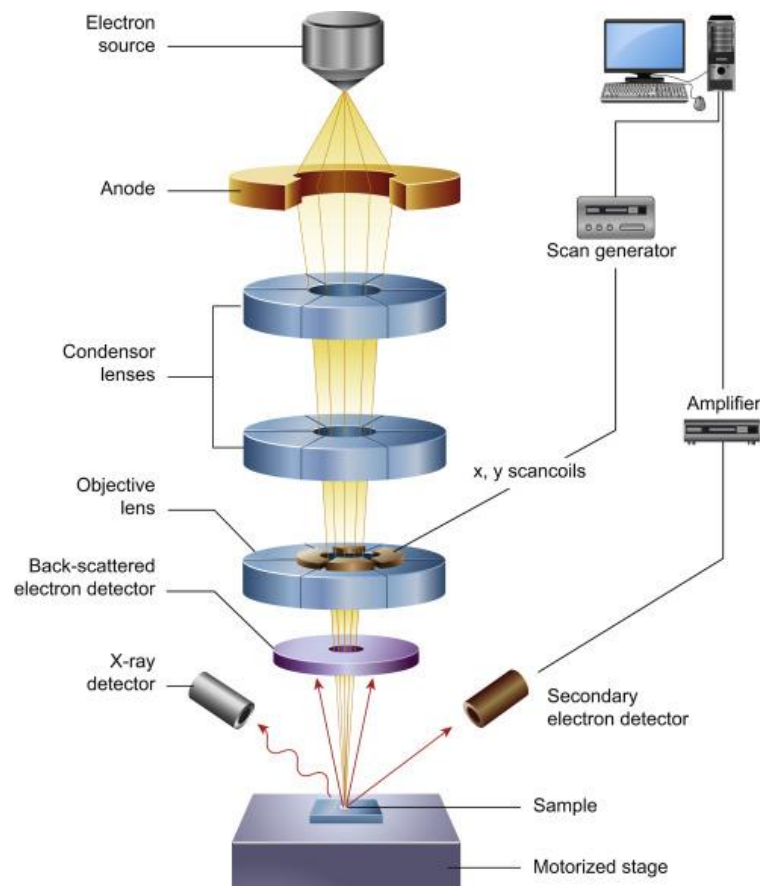


Figure 3.7: Schematic view of a scanning electron microscopy (SEM) apparatus.

Source: Adapted from <sup>64</sup>.

The components of a SEM are basically the electron source (Gun) that can accelerate electrons to an energy in the range of 0.1 to 30 keV, the electron lens that is responsible for controlling the electron path in the evacuated tube, the deflection system which is used to sweep

the beam across the specimen through two pairs of electromagnetic deflection coils, the sample stage and, finally, the detectors for all signals of interest and a display with data output. The detector collects the signal resulting from the beam-sample interaction and the contrast in the image is the variation of this interaction from one point to another. Some essential infrastructure requirements include a power supply, a vacuum and a cooling system, a vibrational-free floor and a room free of ambient magnetic and electric fields<sup>65</sup>. A schematic view of the described SEM apparatus is depicted in Figure 3.7.

### **3.4 Atomic Force Microscopy (AFM)**

Atomic force microscopy (AFM) is a method to imaging the surface of a structure detailed down to the nanometer scale<sup>66</sup>. The advantage of this technique is that it can be done with hard, soft, natural, synthetic, biological materials, regardless of opaqueness or conductivity. The AFM technique is usually called a “blind microscopy” once the image formation is not done by means of light or electrons shadows or reflections. Rather, the AFM is composed by a sharp solid force probe, or the tip. It essentially “touches” the sample’s surface and measures the surface height. The sharp tip is attached to a flexible cantilever that bends when a force is felt by the tip. The bending is measured by a laser that hits the cantilever and is reflected to a photodiode. The position the laser is sensed by the photodiode will be the measure of how to cantilever and the tip moved, constructing the specimen’s surface image<sup>67</sup>. The described components can be seen in Figure 3.8.

In the AFM, the imaging can be done in three different modes. The contact mode or static mode consists of dragging the tip in the sample and the surface is measured using the feedback signal that is needed to keep the cantilever at a fixed position. The second mode is the tapping mode which consists in the cantilever oscillates up and down near or in its resonance frequency usually due to a piezo element in the cantilever holder. Therefore, a tapping AFM image is produced by getting the changing in the tip oscillation when it gets close to the surface, in other words, it is produced by looking at the force of the intermittent contacts of the tip with the sample surface. The third mode is the non-contact mode which the tip does not touch the surface. Instead, the cantilever is put to oscillate in or above the resonance frequency with amplitude of about a few nanometers down to a few picometers<sup>68</sup>. At those amplitudes, van der Waals forces are strong, which, by interacting with the tip, it causes a decrease in the resonance frequency of the cantilever. The laser/photodiode feedback loop system maintain the fixed

cantilever amplitude and frequency by adjusting the distance tip-sample. The measuring of those distances at each point in space results the topographic image of the sample surface.

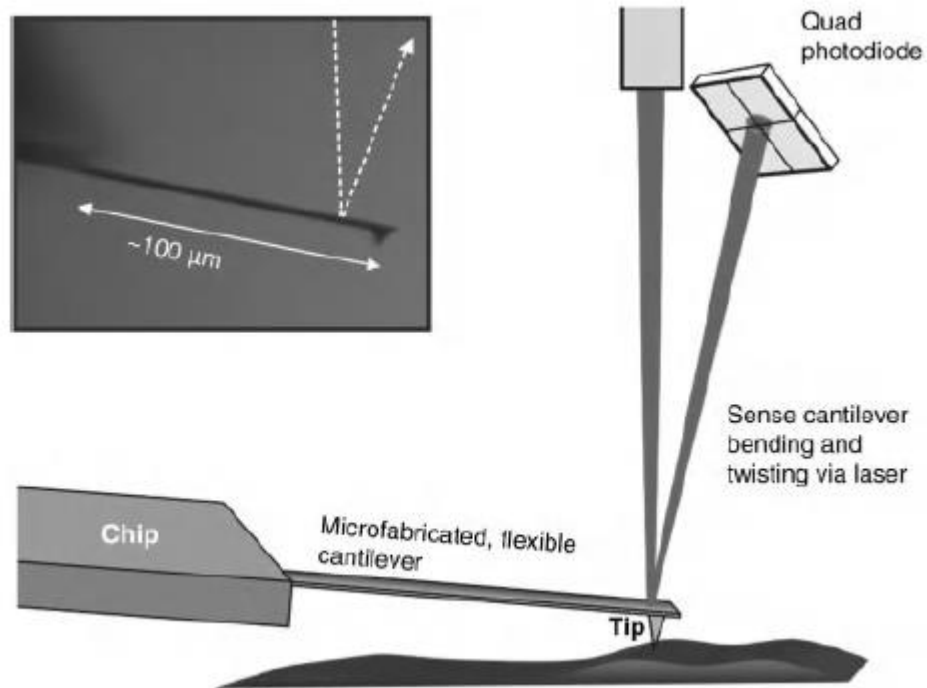


Figure 3.8: Schematic view of the main components of AFM. Inset is a real side view of a cantilever and the tip.

**Source:** Adapted from <sup>67</sup>.

## **4 DECREASING LASER ENERGY THRESHOLD BY VOLUMETRIC SCATTERING DISTRIBUTION ENGINEERING**

Random laser systems are especially interesting due to the vast possible materials to produce those systems. As already mentioned, the materials and architectures of those devices goes from liquid to solid, from organic to inorganic, from thin films to powders and finally, a combination of those characteristics. The material fabricated in this study is placed on the last class. We combine an inorganic matrix to result in a solid-state random laser with an organic dye to work as gain medium and finally, adds titanium dioxide as scatterer centers to provide the scattering required to get a random laser. This is done via sol gel process, a largely used, well known and very cheap technique to obtain solid-state samples. Also, it possesses an easy way to integrate organic dyes once the sol gel technique is a liquid (sol) drying process and the organic molecule in some solvent is easily incorporated to the sol.

A challenge of the random laser field is to achieve a low energy threshold, that is, the amount of energy delivered to the sample needed to the sample to lase. The random laser are good candidates for portable devices because it does not need an external cavity, but it still need a power source to lase, usually a laser with larger dimensions. By getting the energy threshold lower, it would be possible to pump the random laser with smaller lasers, increasing the portability feature.

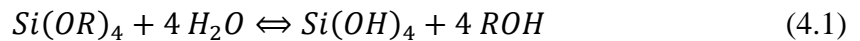
Some random laser devices use particles dispersed in the sample to provide scattering. For instance, X. Meng et.al.<sup>69</sup> showed coherent random laser emission in a weakly scattering polymer device containing silver nanoparticles. S. Caixeiro et.al.<sup>70</sup> proposed a silk-based biocompatible random laser by nanostructuring a porous matrix into the silk proteins. Finally, S. Marinho et.al.<sup>71</sup> also demonstrated random lasing in an alumina porous ceramic infiltrated with Rhodamine B. In all of those works, the scatterer centers are homogeneously distributed. That said, our goal in this work is to investigate if an inhomogeneity of those centers would change the energy threshold. If a decreasing in the threshold happens, it would be possible to decrease the laser threshold of those materials just by performing a scatterer distribution engineering.

## 4.1 Introduction

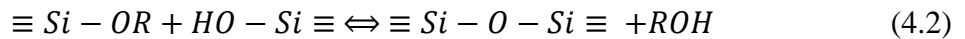
Organic-inorganic hybrid materials have been shown promising to optical and photonic application<sup>72</sup> because they combine characteristics of both class of materials, surpassing limitations they would have individually. Inorganic matrixes are great hosts to solid-state devices and can be synthesized in room temperatures, for example, the sol-gel method, allowing organic dye incorporation, widely used as active medium for laser application<sup>73</sup>. Besides, those organic-inorganic materials present the possibility of nanoparticle incorporation, increasing the scattering mechanism and becoming a good alternative to random laser emission.

As mentioned before, the sol-gel reaction is a method for ceramics and inorganic vitreous preparation at relatively low temperatures. The reaction is divided in two steps: the hydrolyses of metal alkoxides to produce hydroxyl groups followed by the second step, the polycondensation of hydroxyl groups and residual alkoxide groups for the formation of a solid tridimensional structure. Usually, hydrolyses and condensation reactions are simultaneously once the hydrolyses has started<sup>74</sup>. The mentioned reactions are described as chemical equations bellow.

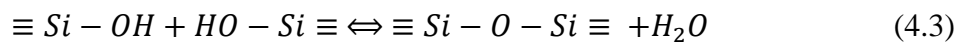
Hydrolyses



Alcoholic condensation



Aqueous condensation



The sol-gel process starts with an alcoholic solution containing the precursor alkoxide with the form  $M(OR)_n$ , which M is the network formation element, in our case, Si, and R is typically an alkyl group, in our case, an ethyl group. In the condensation process, there is a reaction between  $OR - OH$  and  $OH - OH$  that triggers the solid network formation of the form  $-Si - O - Si -$ , leading to formation of alcoholic and aqueous waste. Those sub products are removed from the system by some active process or evaporation, resulting a sample shrinkage. As final product, we have a solid network of  $SiO_2$  tetrahedral named xerogel<sup>75,76</sup>.

## 4.2 Materials and Methods

The samples were prepared via sol-gel method, by aqueous/ethanolic solution utilizing tetraethoxysilane (TEOS) as precursor molecule. For the acid hydrolysis, a solution of 1N HCl in water was added to the mixture. The molar ratio of TEOS/H<sub>2</sub>O/EtOH/HCl was approximately 11:3:3:1. This mixture was mechanically stirred for 2 hours. An ethanolic solution of Rhodamine 6G (Rh6G) was prepared at concentration of 10<sup>-3</sup> M. A mass of 0.3 mg and 1.5 mg of rutile TiO<sub>2</sub> nanoparticles were introduced to 5 mL of the Rh6G solution and taken to ultrasonic bath for 30 minutes in order to homogenize these particles in the solution. In the following step, this aliquot was mixed to 5 mL of TEOS-derived sol. Finally, after drying the sols very slowly at room temperature, xerogels with different concentrations were obtained. The whole procedure is schematically shown in Figure 4.1. Due to the decantation of TiO<sub>2</sub> over the sol-gel process, which takes a couple of weeks, both samples, the lower and the higher concentrated, formed a TiO<sub>2</sub> highly concentrated region at their bottom. For comparison purposes, a sample without rutile scatterers was also produced. The xerogels show cross-sectional dimensions of approximately 4 cm width, 2 cm height and 0.5 mm of thickness. Pictures of the sample without nanoparticles are shown in Figure 4.2. It is observed a clear transparency and the laser pointer excitation in the right handside image is just for fluorescence exemplification, remembering that the laser excitation in the random laser action experiment reaches the sample perpendicular to the face, not parallel, as shown in Figure 4.2(b).

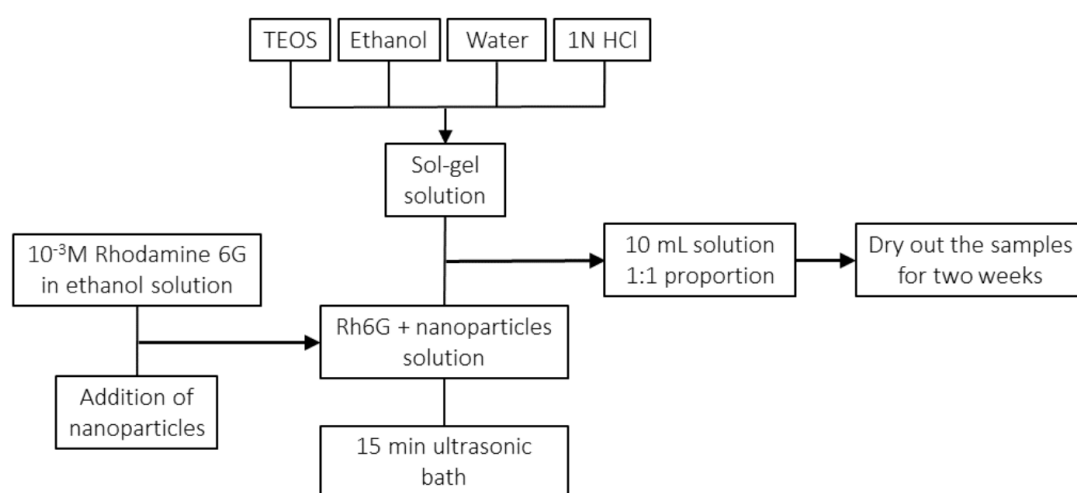


Figure 4.1: Flow chart of the processes to Rhodamine 6G-doped xerogel preparation.

**Source:** By the author.

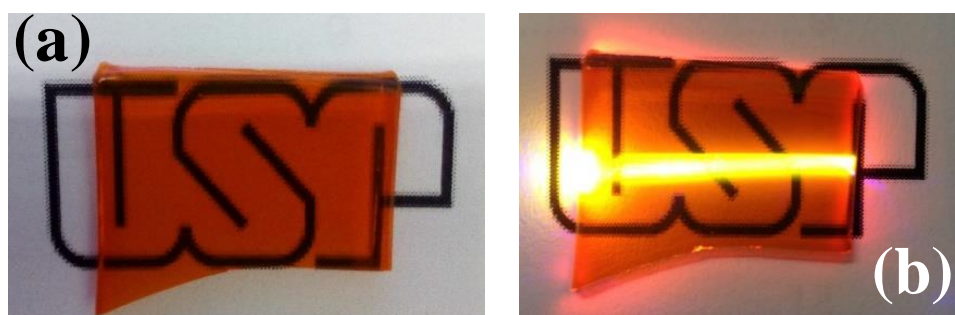


Figure 4.2: (a) Picture of the xerogel sample without TiO<sub>2</sub> nanoparticles. (b) Sample fluorescence by pumping with a 532 nm laser pointer from the left and parallel to the sample surface.

Source: By the author.

### 4.3 Results and Discussion

As described in the experimental section, the decantation of TiO<sub>2</sub> particles over the sol-gel process resulted in xerogels with an inhomogeneous distribution of scatterers. Thus, both samples show a smooth surface and a rough one, as illustrated by the optical microscopy images displayed in Figure 4.3 for the sample with lower concentration of TiO<sub>2</sub> (a-b) and for the higher concentrated one (c-d). Over the smooth face (SF), it is observed a typical superficial sol-gel pattern featuring a few irregularities, which may be caused by either bubbles formed during the sol-gel process or the presence of TiO<sub>2</sub> nanoparticles. Over the rough face (RF), there is a high density of TiO<sub>2</sub> nanoparticles.

By carrying out atomic force microscopy, it was possible to point out different morphology features on the RF of each xerogel, as can be seen in Figure 4.3 (e-f). The average roughness provided by the software, of the RF of sample with higher and lower concentrations of TiO<sub>2</sub> nanoparticles was found to be 48 and 32 nm, respectively, which is two orders of magnitude higher than the 0.2 nm of average roughness obtained for both SF. The size of the morphology features, which can be better visualized in the profile lines of Figure 4.3 (e-f), is about five orders of magnitude higher than the size of TiO<sub>2</sub> nanoparticles measured by zeta sizer technique, meaning that some aggregation of TiO<sub>2</sub> particles took place, thus, the roughness is a result of the rutile scatterers distribution over the RFs. The size distribution of TiO<sub>2</sub> nanoparticles, whose average was found to be  $(350 \pm 60)$  nm, is shown in Figure 4.3 (g). Even though the roughness of both RFs is comparable, their morphology micrographs clearly show

a higher density of scatterers for the xerogel prepared with a higher concentration of  $\text{TiO}_2$  nanoparticles.

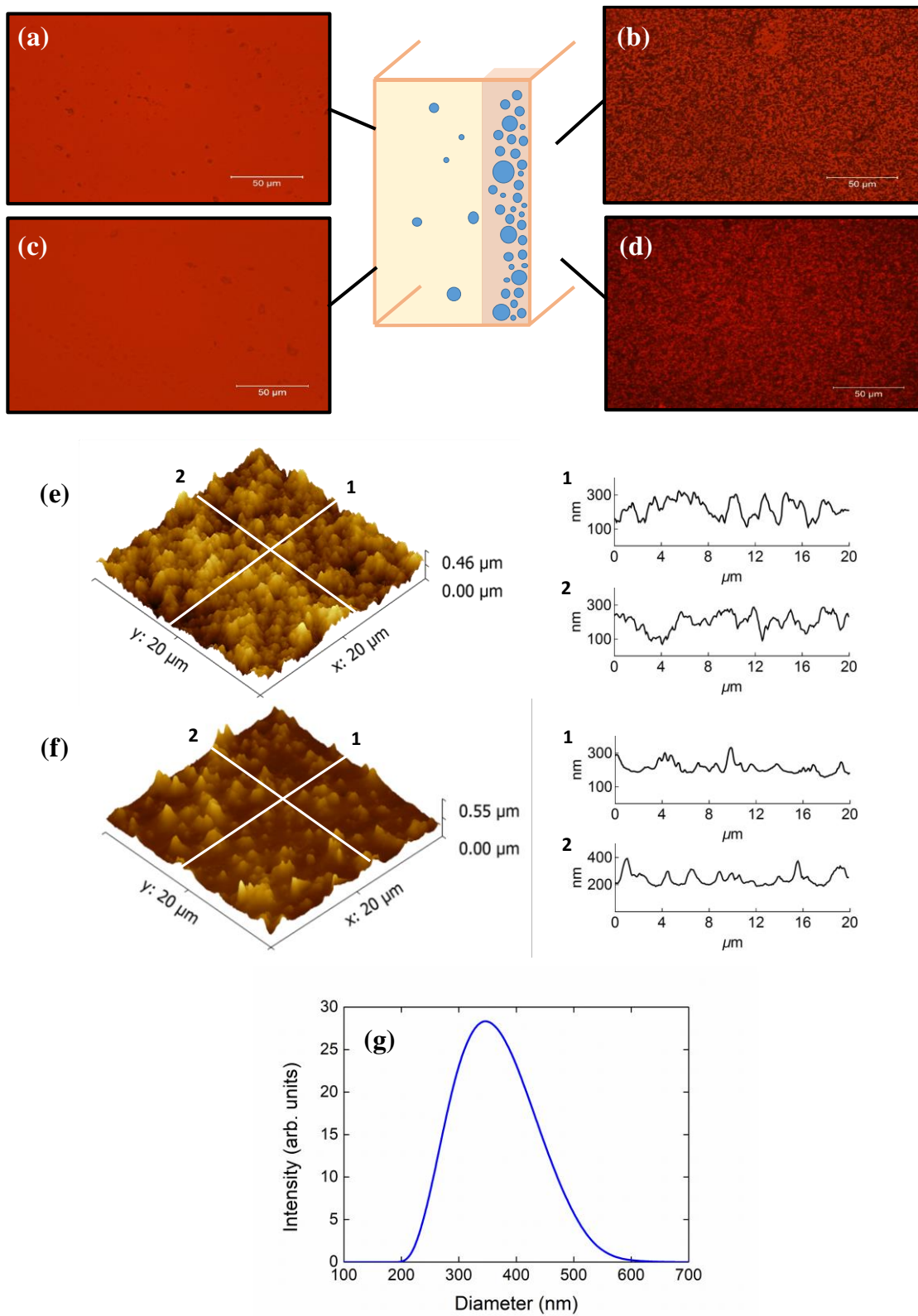


Figure 4.3: Optical microscopy of SF (a) and RF (b) of the lower concentrated sample and SF (c) and RF (d) of the higher concentrated sample. Atomic force microscopy of the higher (e) and lower (f) concentrated sample rough faces (left) and respectively profiles lines (right). (g)  $\text{TiO}_2$  nanoparticles size distribution.

**Source:** By the author.

In order to determine the lasing threshold for the dye-doped xerogels, the integrated emission intensity and spectral linewidth were plotted as a function of pump energy. For the sample without TiO<sub>2</sub> scatterers, these dependences are shown in Figure 4.4 (a-b). A single-peaked emission spectrum showed up and became narrower as the pump energy was increased. A clear lasing threshold was measured at  $(3.6 \pm 0.4)$   $\mu\text{J}$  of pulse energy by fitting the integrated emission dependence on the pump energy to a bilinear curve. Besides, a narrowing effect of 85% was observed in the emission spectrum after the pump had reached the threshold condition. The dominant feedback mechanism in this case, in which no TiO<sub>2</sub> scatterers are present, arises from Fresnel reflections at the sample interfaces. However, scattering at domains with different refractive indexes formed during the sol-gel process may also contribute to amplification of light<sup>77</sup>.

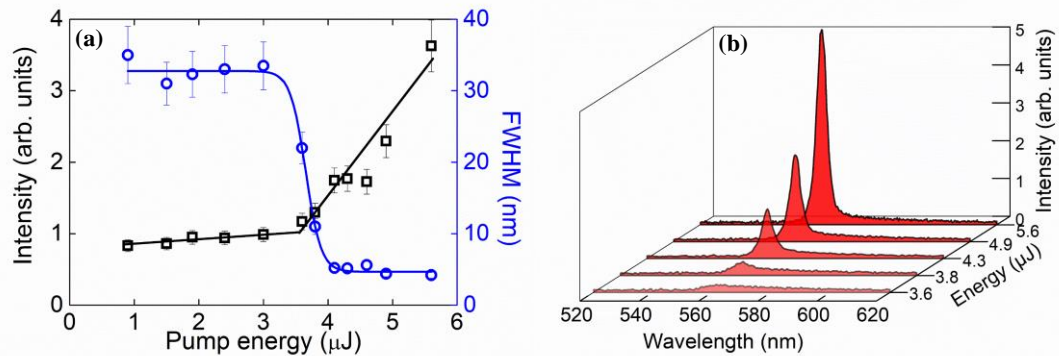


Figure 4.4: (a) FWHM (blue circles) and integrated intensity emission (black squares) and (b) the spectral evolution with increasing pump energies for Rh6G-doped xerogel without TiO<sub>2</sub> scatters.

**Source:** By the author.

Figure 4.5 displays the emission characteristics for the dye-doped xerogel prepared with a lower concentration of TiO<sub>2</sub> nanoparticles. The pump was directed towards its two different faces (SF and RF) at a time, defining two distinguished laser configurations. Thus, Figure 4.5 (a-b) and Figure 4.5 (c-d) show the results obtained by directing the pump to the RF and the SF respectively. Both arrangements exhibited the same incoherent spectral signature, with a decrease of approximately 90% on their linewidth. The lasing threshold occurred at  $(5.1 \pm 0.5)$  and  $(3.3 \pm 0.3)$   $\mu\text{J}$  of pulse energy when the pump was directed to the RF and the SF respectively. When the pump comes in from the RF, a higher energy is required to trigger laser action because a significant fraction of the pump light is scattered off instead of being absorbed by the gain material. The pump light that has not been scattered off has a fraction of its propagation direction rapidly randomized due to multiple scattering as it penetrates the disordered region, thus producing a diffusive volume of excited molecules over the sample.

Under this condition, the propagation direction distribution of spontaneous emitted light does not match the pathways of excited molecules significantly, which also contributes to increase lasing threshold.

On the other hand, when the pump is brought to the sample from the SF, only a small fraction of it is scattered off the gain material, which translates into a lower lasing threshold compared to what was achieved for its architecture counterpart. Once the pump penetrates the sample, it goes along a region with almost no scatters, thus exciting molecules in a confined volume that follows the energy distribution of the pump beam along its propagation direction. As a result, it generates a high energy density of stimulated emission that experiences multiple scattering when it reaches the thin layer of the sample in which the TiO<sub>2</sub> nanoparticles are concentrated. This seed of amplified stimulated emission also contributes to decrease lasing threshold.

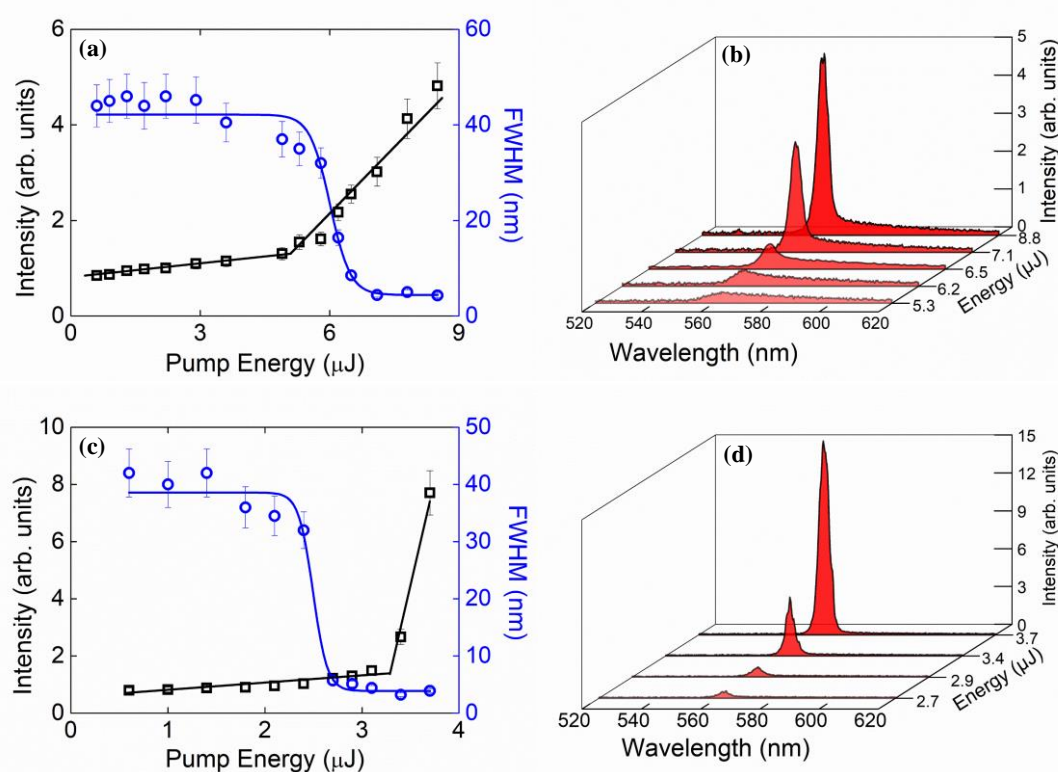


Figure 4.5: (a) FWHM (blue circles) and integrated intensity emission (black squares) and (b) the spectral evolution with increasing pump energies for lower TiO<sub>2</sub> concentration Rh6G-doped xerogel when pumping from the RF. (c) FWHM (blue circles) and integrated intensity emission (black squares) and (d) the spectral evolution with increasing pump energies for lower TiO<sub>2</sub> concentration Rh6G-doped xerogel when pumping from the SF.

**Source:** By the author.

Figure 4.6 displays the emission characteristics for the dye-doped xerogel prepared with a higher concentration of TiO<sub>2</sub> nanoparticles. Again, the pump coming in the two different faces

(SF and RF) at a time provides two laser configurations. Figure 4.6 (a-b) and Figure 4.6 (c-d) show the results obtained by directing the pump to the RF and the SF respectively. Both configurations presented a decrease of approximately 90% on their linewidth, as also observed in the previous sample. When pumping from the RF, the emission exhibited incoherent signature and the lasing threshold occurred at  $(6.7 \pm 0.7) \mu\text{J}$  of pulse energy. A higher energy was required for lasing when compared to the lower concentrated sample pumped at the RF, once now, the fraction of pump light scattered off the sample is higher due to the higher density of scatterers.

On the other hand, pumping the same sample at the SF, the laser threshold occurred at  $(2.8 \pm 0.3) \mu\text{J}$  pulse energy, the least energy required to lasing of all configurations studied. Furthermore, spikes are present in the emission spectra, suggesting a transition to coherent random laser emission. The stimulated emission energy density reaches a high density of scatterers centers, provided by the  $\text{TiO}_2$ , where interference effects are non-negligible, leading to lower energy threshold and presence of spikes in the emission spectra.

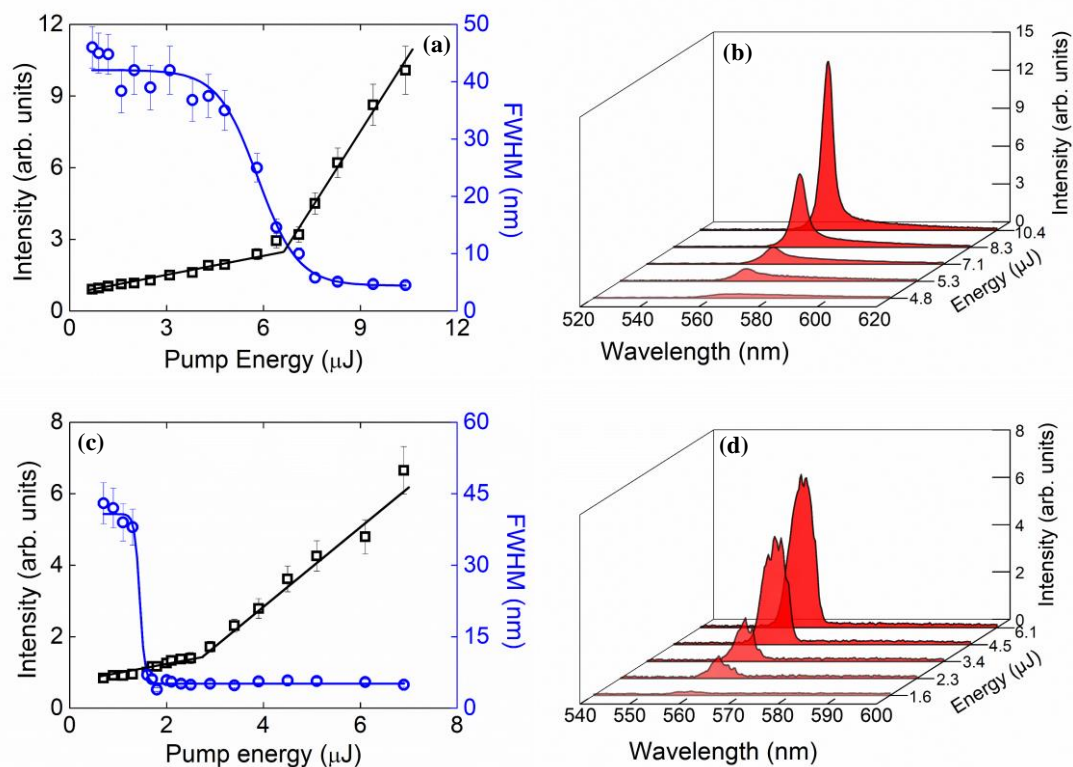


Figure 4.6: (a) FWHM (blue circles) and integrated intensity emission (black squares), (b) spectral evolution with increasing pump energies for higher  $\text{TiO}_2$  concentration Rh6G-doped xerogel when pumping from the RF. (c) FWHM (blue circles) and integrated intensity emission (black squares), (d) spectral evolution with increasing pump energies for higher  $\text{TiO}_2$  concentration Rh6G-doped xerogel when pumping from the SF, spikes are observed.

Source: By the author.

Table 4.1 summarizes the threshold energies for all the configurations measured. As it can be seen, pumping the sample from the RF, the energy threshold increases with the concentration of scatterers. This is associated with the fact that the light reaching the sample is highly scattered, in a way that the amplifying volume is randomized and the energy necessary to get the population inversion is increased.

On the other hand, pumping the same samples in the SF, a reduction of the energy threshold is observed when increasing the scatterers density at the thin layer. In this situation, the light directed towards the sample from a less concentrated face creates an amplifying volume, and, on reaching the concentrated side, scatterers provide the feedback needed to population inversion on the amplifying volume. In this way, increasing the scatterers concentration will increase the intensity of the feedback and, therefore, decrease the energy threshold to laser.

Table 4.1: Energy threshold of the measurements performed as a function of scatterer concentration of the sample.

|                      | SF threshold ( $\mu\text{J}$ ) | RF threshold ( $\mu\text{J}$ ) |
|----------------------|--------------------------------|--------------------------------|
| No scatterers        | $3.6 \pm 0.4$                  | $3.6 \pm 0.4$                  |
| Lower concentration  | $3.4 \pm 0.3$                  | $5.1 \pm 0.5$                  |
| Higher concentration | $2.8 \pm 0.3$                  | $6.7 \pm 0.7$                  |

We can get a better visualization of the processes occurring in the sample by analyzing then as the flux of pumping photons and emitted photons go through the sample from the pumping incident surface to the output. Firstly, by looking to the pumping in the smooth face, we can observe that the incoming photons flux encounters a region with low scattering region, which permits a high excitation volume inside the sample surface. Once a high volume of molecules is excited, it will result in a rate of spontaneous emission. A fraction of those emissions will get to the highly scattering portion of the sample. There, once the frequently scattering processes will promote a low photon diffusion, the stimulated processes will have enough time to get laser amplification. Depending on the degree of scattering processes, there could be even the formation of loops and the coherent random laser emission. Those steps are schematically shown in Figure 4.7.

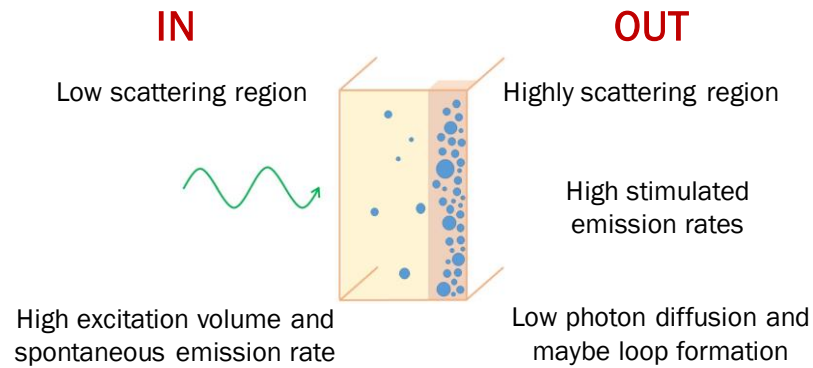


Figure 4.7: Schematic view of the absorption, scattering and emission processes for the case of pumping in the smooth face.

**Source:** By the author.

On the other side, the processes occurring by pumping the sample from the rough side is shown in Figure 4.8. Firstly, the incoming pumping photons get to a highly scattering region, in a way that some of the pumping intensity is scattered out of the sample even before being absorbed by the molecules. Also, the excited volume in the sample is diffuse once the pumping photons can be scattered before it is absorbed by a molecule. It results in a diffuse and low rate of spontaneous emission. Besides that, when emitted photons get to the opposite side of the sample, they experience a low scattering region which makes the light quickly leave the sample volume and resulting in a low amplification. Due to those processes, the pumping energy required to reach amplification and further, random laser emission, will be larger than compared to the previous case.

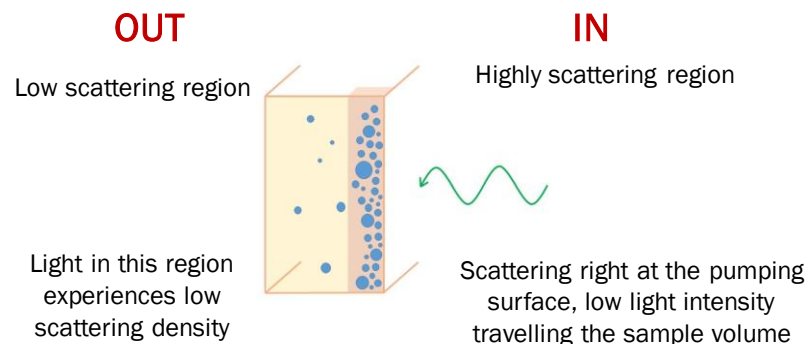


Figure 4.8: Schematic view of the absorption, scattering and emission processes for the case of pumping in the rough face.

**Source:** By the author.

When dealing with homogeneously scattering distributions, we will have some degree of roughness in both sample's surfaces in a way that a portion of the incoming pumping beam will be scattered off the sample. Also, once the scatterers are homogenous in the sample volume, right after the surface, the excited volume will be somehow diffused due to the scatterers in there. So, disposing the scattering centers in the way it was done in this work will present some advantages. In our architecture, the excitation volume promoted by the pumping beam will be uniform and more efficient in terms of excited molecules and the total losses in this specific process will be decreased compared to the homogenous sample. Second, the highly scattering region supports coherent emission even this region been a small volumetric portion of the total sample volume. To reach the high density characteristic in a homogeneous sample, it would be necessary to get all the sample volume in this level of density, which will require a high quantity of scattering centers. This requirement will both raise the cost of production and sometimes the high mass of scatterer in the sample preparation can be difficult for the solid formation in the case of solid state random lasers.

## 4.4 Conclusion

Besides the random laser emission observed in a Rh6G-doped TEOS-derived xerogel without TiO<sub>2</sub> nanoparticles, the energy threshold of TiO<sub>2</sub>-doped matrixes was observed to depend on the samples' side where excitation takes place owing to the inhomogeneous TiO<sub>2</sub> distribution due to decantation that occurs during sample preparation. By adding scatterers centers, the laser threshold energy decreased by 22% when pumping from the SF compared to the sample without nanoparticles due to the multiple scattering amplification of the stimulated emission at the TiO<sub>2</sub> thin layer. On the other hand, pumping from the RF side, the laser threshold energy increases 85% due to scattering of the excitation light off the sample and the randomization of spontaneous emission not matching the excited molecules.

The interesting consequence of the study is related to the fact that the way the scatterers are arranged in the sample volume alters the laser threshold, therefore, it would be the case that the homogeneous arrangement might not result in the lowest threshold. So, a scatterer arrangement engineering aiming the increasing of the scattering strength could be a way to lower energy threshold in random lasers, which is one of the present challenges in this area to microchips and lab-on-a-chip applications once it requires a certain degree of portability and the necessity of a commercial laser to pump the random laser would be impractical.

A further investigation would be comparing those energy thresholds to a sample with homogeneously distribution of scatterers. In the case of this work, it was not possible because the decantation of the  $\text{TiO}_2$  used is eminent. A way to work around that would be using a different scatterer that present a really slow decantation such that would be possible to control the scatterer dispersion in the sample by accelerating or slowing down the drying process.

## 5 FLEXIBLE POLYMERIC FIBER RANDOM LASER AS POTENTIAL THERMAL AND CHEMICAL SENSOR APPLICATION

One of the breakthroughs of the random laser is the capacity of lase without any mirror cavity. It grants a level of portability never experimented before for lasers. In addition, the cheapness of those systems are incredible, could be even disposable. Once no mirrors and alignments are needed, for a random laser, one just have to fabricate a highly scattering sample. Therefore, it is the first time it is possible to get a mass production of a laser system. Also, the newest technology industry is going forward to the development of elastic, stretchable and flexible responses such as smart skin and wearable devices<sup>78,79</sup>. In the photonics field, the random lasers are the class of laser that possess those features, mainly using polymer<sup>80</sup> and graphene-like materials<sup>81</sup>.

Those characteristics leads to a clear direction of using those systems as sensor applications. Furthermore, the random laser emission features strongly depends on the scattering properties of the medium, so, it could be used to sensor different scattering media that alters with variations in the medium disorder<sup>82,83</sup>. In this work, the sensor is based on a statistical treatment called the Pearson correlation coefficient of the emission spectra. On the random laser field, this treatment is used in the last decade to study mode interactions by analyzing the correlation between them<sup>63,84-87</sup>.

On our new approach, we intend to apply this statistical tool not only to try to understand how the laser modes interact in a non-cavity laser system, but to use as a tool to monitor the emission features in a large time of pumping by producing correlation maps from time to time using an ensemble of spectra, each one taken at a pumping shot of the pulsed laser.

### 5.1 Introduction

The fibers studied in this thesis were fabricated via electrospinning technique. It is based on the principal of electrostatic attraction of charges. A polymeric solution is placed inside a syringe that will pump the solution to the needle. The tip of the needle and the collector are supplied by a high voltage power. The high voltage makes the solution in the syringe to overcome the surface tension and form a cone like structure called Taylor cone. The fibers

resulting from the Taylor cone is collected by the collector<sup>88,89</sup>. The schematic diagram of this process is illustrated in Figure 5.1.

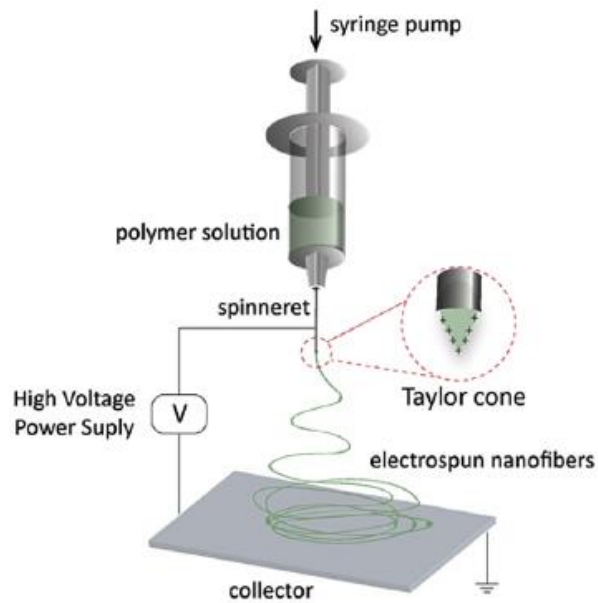


Figure 5.1: Schematic diagram of a typical electrospinning apparatus setup.

**Source:** Reprinted from<sup>90</sup>.

The main advantages of producing fibers network with electrospinning are the simplicity, low cost and short time of the processing system and the possibility to obtain fibers with diameters between 0.1 to 1.4  $\mu\text{m}$ , providing Mie scattering of light and light guided direction, which is important to random laser applications. Alongside, this technique allows the fabrication of organic/inorganic composite systems, permitting dye incorporation that can serve as laser gain medium<sup>90</sup>.

Electrospinning-based (bio)sensors has been established as a promising approach for the development of smart, miniaturized, portable, ultra-sensitive systems in the use of agriculture and food analyzes. These features are also desirable in random laser devices. Random laser systems do not require mirror cavities, which promotes then as great portable systems. The next step would be the fabrication of portable systems at low costs, promoting then to a disposable device. For sensor devices, this is a good characteristic once the sensing process can damage the material<sup>91</sup>.

This is the objective of using the fiber fabricated via electrospinning technique in this case. It was possible to use the random laser emission of those fibers to probe, for example, a sub nanometer line widening of the laser emission. It could be used as a sensor for the presence

different types of polymeric degrading substances in the air that damaging the fibers alters the random laser emission profile and we can detect sub nanometer changes in the profile.

## 5.2 Materials and Methods

The reagent polymethylmethacrylate (PMMA,  $M_w = 350,000$ ) was acquired from Sigma-Aldrich and the reagents Rhodamine B (RhB) and chloroform was acquired from Synth (São Paulo, Brazil). Solutions containing PMMA and Rhodamine B was prepared via dissolution in chloroform of 5% (m/V) of PMMA and 5% (m/m with respect to the PMMA) of Rhodamine B. It was kept under stirring for 2 h in room temperature. The PMMA/Rhodamine nanofibers was obtained by electrospinning technique, applying a flow rate of  $0.15 \text{ mL}\cdot\text{h}^{-1}$ , an electric voltage of 20 kV, working distance of 6 cm and spinneret internal diameter of 0.8 mm. The nanofibers were directly collected in glassy substrate.

The morphology and diameter of the fiber was analyzed by a scanning electron microscopy (SEM) (JEOL 6510) for imaging, after covering the sample surface with gold aided by a metallizer (Laica, EM SCD050). The fiber diameter was evaluated through an image analyzer software (Image J, version 1.47a). The average diameter and respective distribution was determined by analyzing approximately 100 fibers.

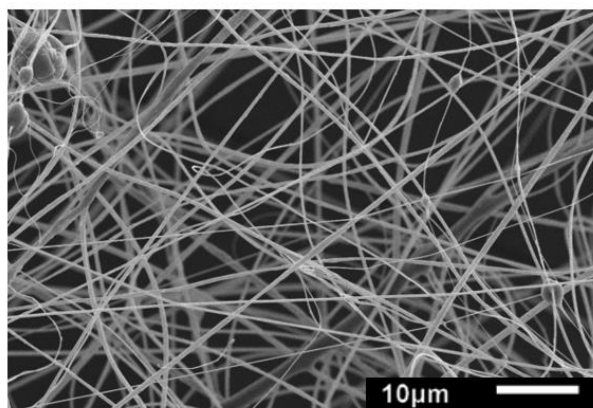


Figure 5.2: MEV image of the 5% (m/m) Rhodamine B-doped PMMA nanofiber.

**Source:** Provided by Embrapa.

Figure 5.2 show the SEM image of 5% (m/m) Rhodamine B-doped PMMA nanofiber. It can be seen that the obtained nanofibers present no porosity or surface defects and some beads. The average fiber diameter was  $(4,78 \pm 0,54) \times 10^2 \text{ nm}$ . Since the Rhodamine-B emission band is about 610 nm, the scattering effects are related to the Mie scattering, which results in a

highly scattering sample for the Rhodamine B emission. Furthermore, the presence of beads and the fact that the fibers are randomly placed in the substrate provide an increasing in the scattering processes. In this case, the fiber morphology acts as the scattering medium and the Rhodamine B molecules in the fiber as the gain medium. So, light propagating in this medium are absorbed, emitted and scattered by the same media, that is, the RhB-doped fibers.

A sample prepared with 1% (m/m) of Rhodamine B was also studied in this work. The fabrication parameters are the same used for the 5% doping sample. The fiber MEV images and sample diameter measurements are in progress and, therefore, are not shown in this thesis.

### 5.3 Results and discussions

The spectra obtained for the 5% RhB sample are quite varied for different regions of excitation as can be seen in Figure 5.3. We can see that both coherent and incoherent random laser can happen with different number of spikes. The peak emission also differs from shot to shot, been from 595 nm from an incoherent emission to peaks of a coherent emission appearing in 625 nm. As already mentioned, the large emission band of the dye promotes photon from different spectral positions to be stimulated amplifying. The various emission profiles are expected in this sample morphology once the fibers are arranged in a completely disordered manner, with portions of the sample containing different densities and dispositions of fibers as they were deposited randomly in the substrate, so that distinct excitation areas leads to different possible modes lasing. This feature leads to both incoherent and coherent spectra with few or many laser peaks depending on where the excitation takes place.

Fixing a region of excitation, the behavior of the emitted light as a function of the pump energy was obtained by integrating the emission intensity over the lasing spectrum for several pumping energy values. A laser threshold was measured at approximately 1  $\mu\text{J}$  of pulse energy, which is comparable to other random laser fiber materials in the literature<sup>92,93</sup>. The result and the emission spectrum evolution as the excitation increases are depicted in Figure 5.3. It is observed that by increasing the energy delivered to the sample, the number and intensity of the peaks also increases. The extra energy allows another mode to lase or already lasing modes to increase its intensity. We can also realize that from pumping energy of 3  $\mu\text{J}$  forth, the emission intensity linearly increases, showing a saturation of the lasing modes. The lasing modes are about the same in this energy range, only the intensity of the preexisting modes increases linearly.

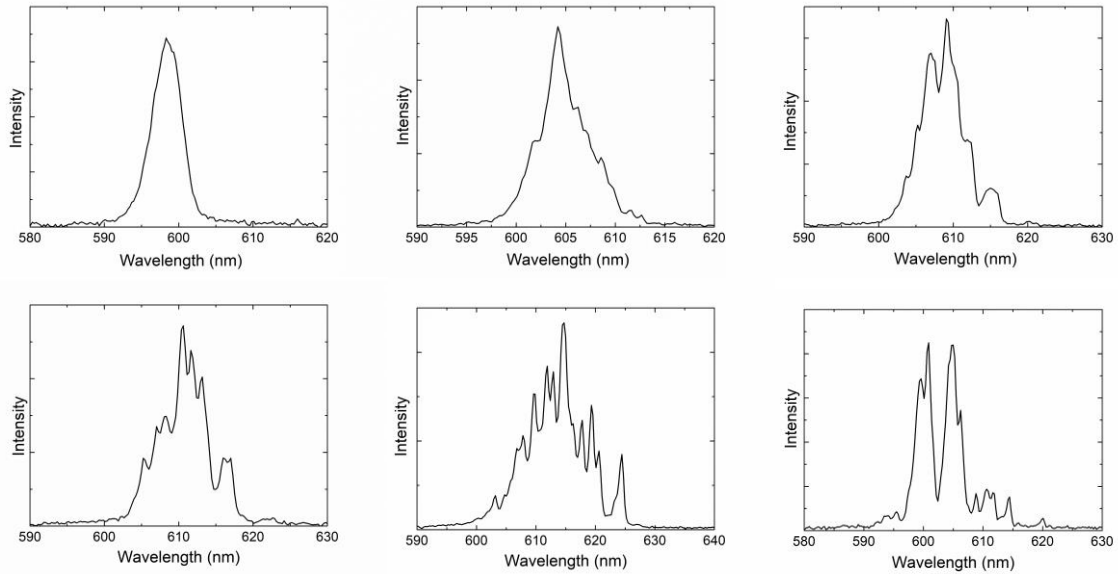


Figure 5.3: Emission spectra from different regions of excitation in the sample. The pump energy and spot area are fixed. Coherent and incoherent emission are acquired.

**Source:** By the author.

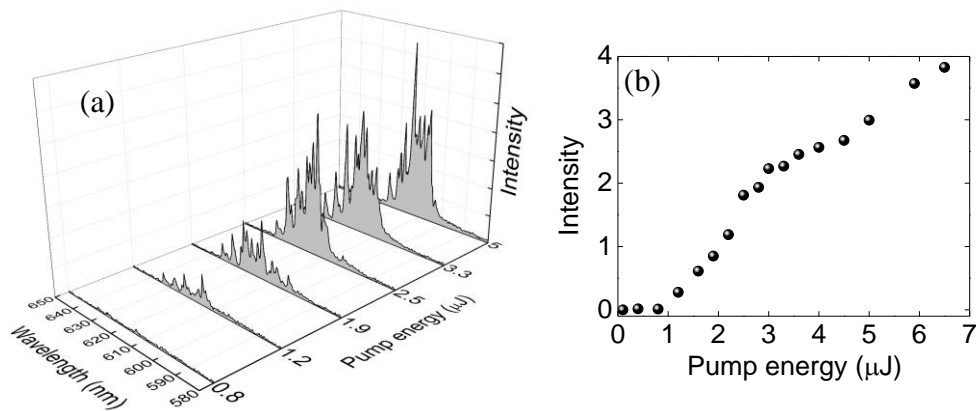


Figure 5.4: (a) Emission spectra of the Rhodamine B-doped fiber for increasing pump energy. (b) Integrated intensity of the emission for increasing pump energy, a laser threshold is reached about  $1\mu\text{J}$ /pulse.

**Source:** By the author.

Another feature was the emission spectra remained unchanged from shot to shot when the excitation region and the energy delivered to the sample was fixed, showing that, despite the chaotic arrangement of the fiber network, the lasing modes from the open cavities formed in the excited area are always the same. It is interest to note that consecutive shots are independent from each other, that is, the shot to shot time of the pumping source is usually 50 ms while the Rhodamine B molecule presents an excited state lifetime on the order of a few

ns<sup>94</sup>. Therefore, the excitation, scattering and emission features due to a shot of the pumping laser completely vanishes long before the next pumping shot hits the sample.

There are some sub nanometer changes in the emission spectra after applying hundreds of excitation pulses on the sample, probably due to degradation of the dye or morphological changes of the host material as can be seen in Figure 5.5, where the spectrum number 500 has a maximum of 0.8 nm peak shifting comparing to the first six spectra taken. In fact, by calculating several C correlation maps between the emission number 1 and 500, it was possible to monitor the dynamics of the lasing modes shift, proving to be a sensitive technique to detect almost imperceptible changes in the emission peaks from long time sample exposure.

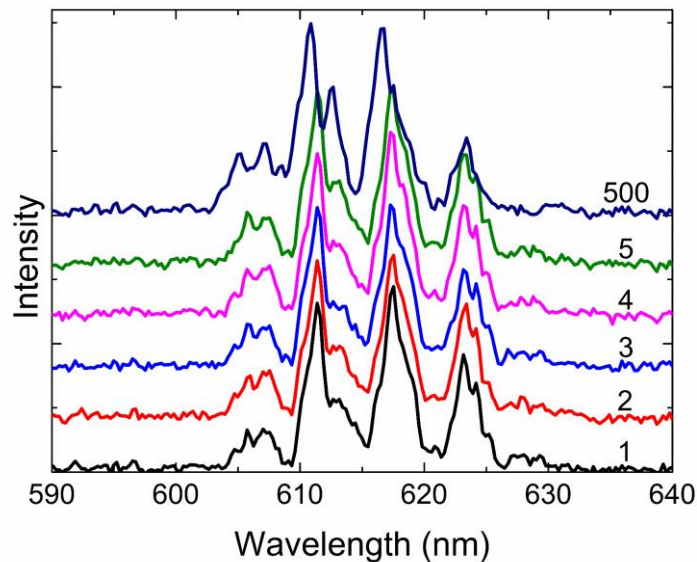


Figure 5.5: Emission spectra of the first five pump pulses and the emission spectra of the pump pulse number 500. A long time excitation caused a subnanometer difference in the emission.

**Source:** By the author.

By producing the 2D correlation map from an excitation area that leads to an incoherent emission and another map by pumping in an area where coherent behavior is observed, we demonstrated the mode-locking transition, which was already shown in a recent paper<sup>63</sup>. One of the tools used to demonstrate it is the PCC, which was already employed in some papers<sup>84,85,87</sup> to study mode correlation of coherent emission. The mode-locking transition states that if fluctuations of the intensity of certain peaks in the emission are correlated shot-by-shot, then these peaks belong to the same resonant mode. In terms of correlation map, the transition consists on a highly correlated region (almost a unity) concentrated in the wavelengths where the peak emission is centered when analyzing the incoherent emission. The coherent emission

map presents a high value of C coefficients ( $> 0.7$ ) dispersed in the entire map, meaning each mode in the emission spectrum is correlated with the others. By comparing the emission spectrum with the correlation map, we can see that between the coherent peaks (valleys), the correlation values are less than average once at these wavelengths there is no mode lasing, and therefore, no interaction with the other modes, as we can see in Figure 5.6. Both correlation maps were performed using a total of 100 spectra acquired at 20 Hz of laser repetition rate. Also, the pumping laser energy was set to be just above the energy threshold for each case, approximately at  $2 \mu\text{J}$  per pulse.

It is important to state that the work<sup>63</sup> showed that this correlation coefficient transition is associated with the mode phase locking by using a coupled mode theory (CMT). In this work, the mode-locking transition was achieved by changing the pumping area profile from a strip-like pumping to a circular spot pumping. In their CMT model, the spot profile changing is mapped by modifying the input of the number of resonances to which every mode couples. When the number of modes increases, the relative phases between them gets constant and, the spectrum goes from a high number of peaks to a lower one (coherent to incoherent emission) and the average correlation coefficient C increases ( $\sim 0.4$  to almost a unity).

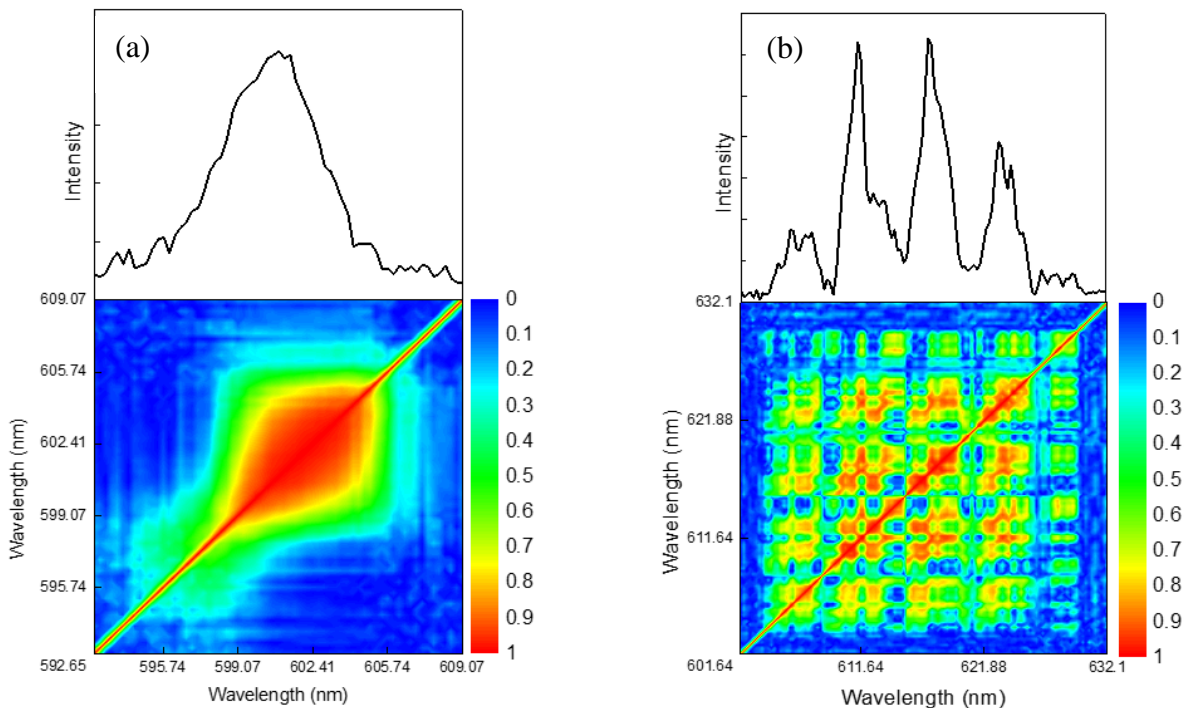


Figure 5.6: Correlation map for an incoherent (a) and coherent (b) emission by pumping the sample in two different. On top of each map, the spectrally correspondent emission spectra for a pump shot.

**Source:** By the author.

In our approach, only by selecting regions where incoherent and coherent random laser were possible due to sample's irregularities, we could observe the mode-locking transition, in contrast with a mode-locking transition in polymer fibers which the coherent feedback occurred only in a TiO<sub>2</sub> doped sample while an incoherent emission occurred on an undoped one<sup>84</sup>. Our result of a correlation between peaks stands for all the places of the sample we collect coherent emission, the one plotted here is an example of the usual map we get from the measurements.

The subnanometer changes in the emission spectra for hundreds of shots motivated the production of maps with the same number of shots. The idea is to split the total time from the first to the last shot in equally spaced time intervals. Therefore, it would result in a series of "photos" of the modes lasing and by comparing then, it would reveal when in time a certain mode lases or stop lasing. The only hardship is the fact that the statistic requires a certain amount of emission spectra to be trustworthy, which constrains the possibility of making maps close in time. However, for a large number of spectra (thousands of them), it would be positive once now we would analyze only a few maps instead of thousands of spectra. In addition, once the changing in the spectra requires a large number of shots to happen, there is no need to evaluate each one of the spectra and compare to the next one.

Instead of looking for a correlation map for 500 emission spectra, for example, we propose to perform five maps of 100 successive pumping shots, as shown in Figure 5.7. Each map was produced by pumping the sample in 20 Hz of repetition rate, resulting in 5 seconds of monitoring for 100 spectra. For a total of five maps, the total time of mode competition analyzes is a total of 25 seconds. Therefore, it was possible to monitor the shift in the emitting modes and to know where in time the more intense modes are more or less mode-locked. As an example, the mode around 627 nm, in the first correlation map, losses the intensity as the two following maps become blue in this particular region. On the other hand, a mode emerges at the last map around 630 nm. Another feature presented in the maps are the strength of the modes correlation, which increases in the third and fourth maps for the two central peaks. It means that for this specific amount of time (from the first and last shot used to perform the graph), the two central modes are highly correlated and no degradation or morphological changes affected their interaction.

It is worth notice that even for a mode that have low relative intensity, the correlation map is capable of differentiate it from noise, once it is a statistical tool, it does not take into account the intensity fluctuations of the excitation laser. So, it can be used to map small changes in the emission spectra that would be difficult to analyze spectrum by spectrum. For example, studying the dynamics of emission line widening and blue or red shift caused by degradation

or changes in the local environment. In our case, we force the pumping laser itself to causes it, but it could be the case of external factors as temperature changes, chemical environment changes, etc. As the random laser does not need a cavity, the fiber material studied could be placed in hostile surroundings where concentration of some substance that interacts with the fiber changing its emission spectra are evaluated by monitoring how fast those correlation maps changes.

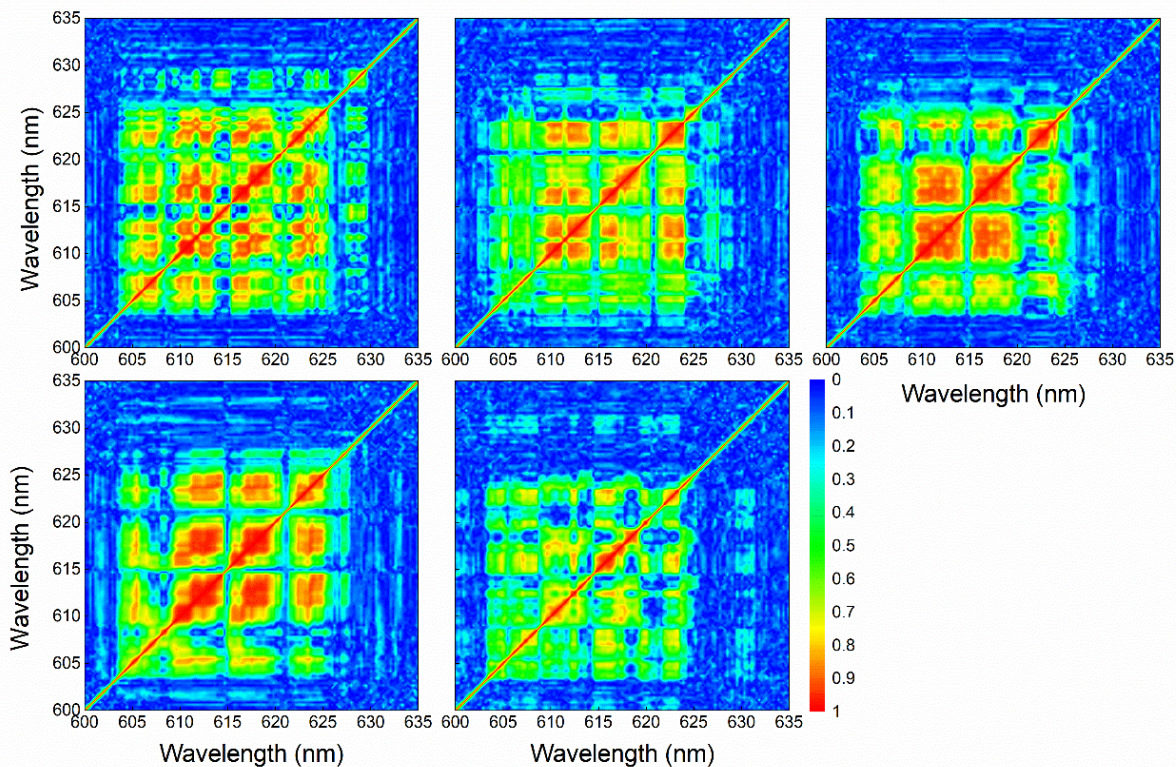


Figure 5.7: (a) Pearson correlation map for the coherent emission from each 100 shots taken in 500 shots evidencing the mode competition as a function of time.

**Source:** By the author.

To test this hypothesis, we measured a set of incoherent emission spectra presenting a widening of half a nanometer in 500 shots acquired at a rate of 20 shots per second, resulting 25 seconds of monitoring and the resultant correlation maps precisely account for the dynamics from every hundred shots collected, which can be seen in Figure 5.8. The increasing of the red areas in peripheral wavelengths in the map represents the frequency widening of the emission, which is related to the fact that, over time, wavelengths that were just noise in the early shots resulting a blueish region in the graph, now presents a non-zero intensity emission due to the widening of the emission band. Once now there is signal from the sample in those wavelengths, the correlation between then and other wavelengths of the emission band starts to increase and approaches one as the number of the emission spectra is growing because, after a large amount

of shots for example, there will be a few shots in the beginning of the measurement that it was just noise at those wavelengths and the rest of the spectra, the widening transforms noise in emission intensity and it will account for the C value to gets to one.

For instance, let's say that in such experiment, 1000 shots were taken and a widening of the emission band happens throughout the time the maps are calculated. Suppose that in the first 100 shots, the band widening makes the sample emits in some wavelength that it was not emitting in the first shots. For simplicity, let say that in shot 50 the noise became an emission at that wavelength. So, in the map of the first 100 shots, the C value at this particular wavelength will be calculated based in 50 shots of completely randomness ( $C \sim 0$ ) and 50 shots that has some correlation, let's say 0.3. Now, due to continuously widening of the emission band, the intensity at the considered wavelength will never be noise again. Thus, the map at 1000 shots, we would have the first 50 shots as noise and another 950 shots of some correlations, resulting a C value approximating 1, once now 95% of the shots are somehow correlated at this wavelength. This is exactly what happens to the maps in Figure 5.8 as the peripheral areas of the band increases its red area from map to map.

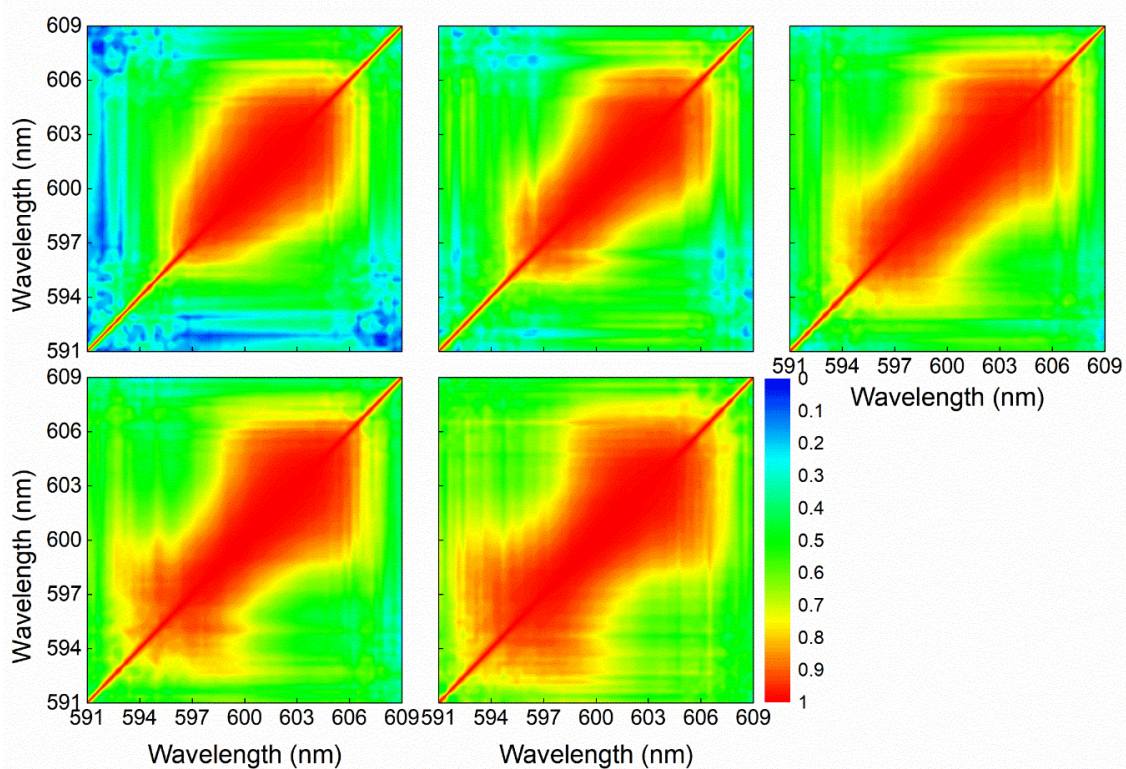


Figure 5.8: Pearson correlation map for an incoherent laser emission from each 100 shots taken in 500 shots total. A clear line widening dynamics is observed.

**Source:** By the author.

For elucidation, we compared some of the normalized emission spectra that results those maps of Figure 5.8. For instance, we take the first three emissions and plotted together with the last three emission spectra of 200 shots, as shown in Figure 5.9 (a). It is clear that without the curve labels, it is impossible to distinguish the first and last shots caused mostly by the laser power oscillation. So, besides the difficulty of analyzing hundreds of emission spectra to search for emission band widening, observing the existence of such phenomena is sometimes almost impossible by this method. Furthermore, we can see in Figure 5.9 (b) that the three first and last shots of a total of 500 shots, the emission spectra became more distinguishable mainly at the  $\sim 603$  nm. The separation between those spectra are on average  $\Delta\lambda \sim 0.4$  nm. Even though it is still a subnanometer change, we can see in Figure 5.8 that the red are of the fifth map also enlarges even more when compared to the second map.

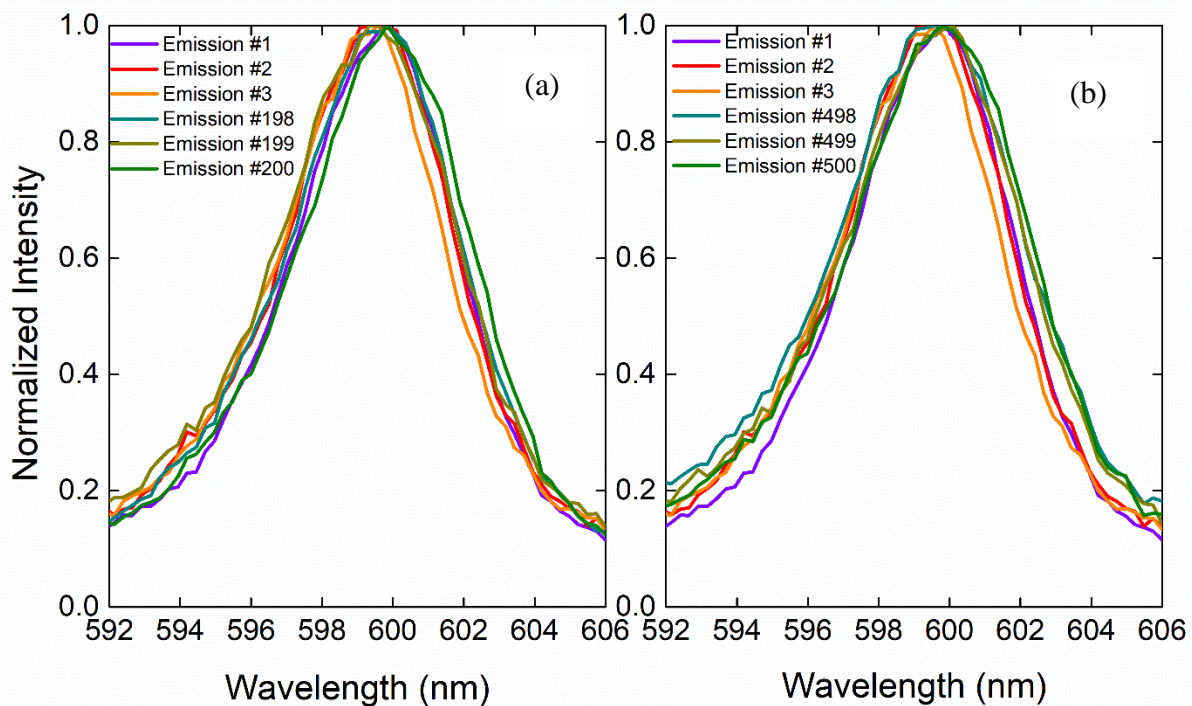


Figure 5.9: (a) Spectral comparison of the first and last three emissions in the first 200 shots and (b) spectral comparison of the first and last three emissions in the 500 shots taken showing the subnanometer line widening of the emission.

**Source:** By the author.

We can go further, by increasing the laser repetition rate, it was possible to provoke a higher and faster degradation, and observe how the correlation maps responds. Once the correlation map method proves to be extremely sensitive for getting information of emission band widening, what a map would results if the widening was much stronger and faster, also,

what if the spectra present a redshift or blueshift. For this particular study, it was used the same polymeric matrix but this time with 1% (m/m) of Rhodamine B as organic dye with the same preparation process described for the 5% (m/m) one. A characterization of the laser threshold and FWHM of this new sample, as depicted in Figure 5.10 was done resulting a laser threshold of about 2.5  $\mu\text{J}/\text{pulse}$ , which is 2.5 times higher than the laser threshold for the sample doped with 5% (m/m) Rhodamine B probably due to the 5 times lower concentration of the dye. Another interesting fact about this sample is that the emission never presented coherent properties. For all the positions of the pumping laser at the sample tested, all the emission spectra were with no spikes. It is not fully understood the reasons for this. A possibility is the amount of Rhodamine in the sample that restricts the possible light paths in a way that the chance to produce a spike is virtually zero or the presence of a lower concentration of Rhodamine in the polymeric solution could decrease the degree of randomness of the fibers during the process of fabrication. The last possibility would also explain the higher threshold once the decrease of randomness leads to a lower degree of scattering and therefore, requires a higher pump energy to achieve the random laser emission.

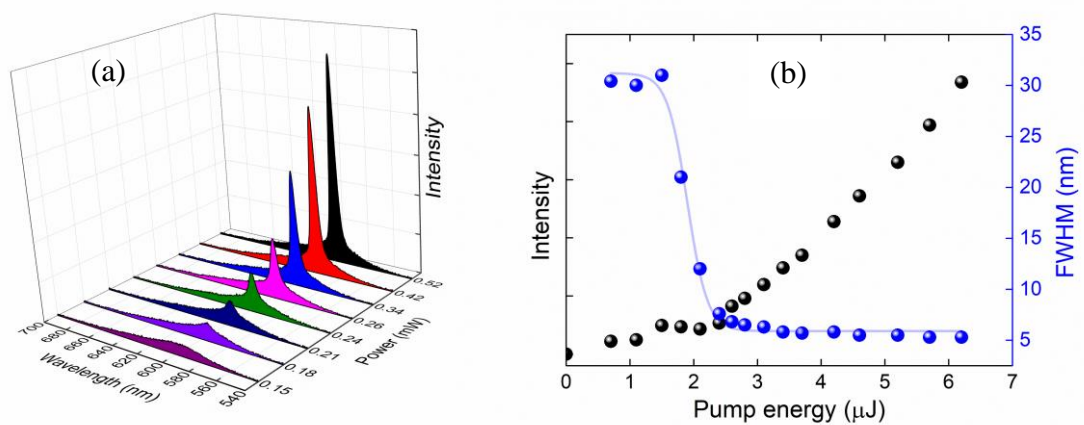


Figure 5.10: (a) Incoherent random laser emission spectra and (b) integrated intensity and FWHM as a function of the pumping energy. Threshold is observed around 2.5  $\mu\text{J}/\text{pulse}$ .

**Source:** By the author.

As already mentioned, the degradation in this case was promoted by heating the sample due to the laser operating at 100 Hz of repetition rate. We produced 500 emission spectra acquired shot to shot, monitoring the sample for a total of 5 seconds (1 second per map) in a way that one shot is separated to the next one by 10 ms. The first step is to analyze the correlation map for the first 100 shots, shown in Figure 5.11 (a). We can see in the correlation map that a line widening occurred as the red area of the lower and higher wavelength are

broadened. This would be the expected evolution of the correlation maps shown in Figure 5.8 if the widening was larger.

The solid line square in the correlation map highlights a region that we have a negative correlation represented by the blue color that was not present in the previously maps. Remembering that a negative correlation is related to a high correlation but with a line with negative slope coefficient. We can understand this phenomenon by analyzing what is happening with the emission curves shot by shot. In Figure 5.11 (b) is shown the first and last curve of a total of 100 shots analyzed. All the intermediary curves would lay between them. Also, the wavelengths between the dashed lines in the map is the gray regions in the emission spectrum.

We can see that due to the blueshift of the spectra of about 1.3 nm peak to peak, the left gray region is decreasing in intensity while in the right gray region, the intensity is increasing. So, if we would plot the intensity for a wavelength of the left region and one in the right, it would result in a negative slope line. This is exactly what means the C coefficient, leading to a  $C < 0$ . Besides the information that a widening is occurring monitoring the spread of the red region in the corners of the map, we also can tell that a band shift is occurring by observing the appearance of negative correlation regions.

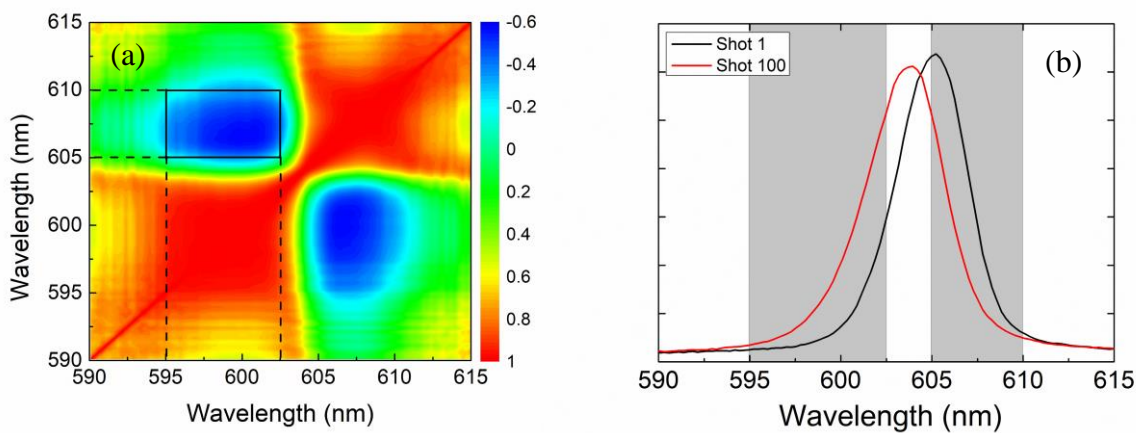


Figure 5.11: Pearson correlation map of the first 100 shots (a). The area highlighted by the square is a negative correlation region between wavelengths marked amid the dashed lines. The first and last emission spectra of the set of spectra considered (b). The gray areas are the dashed lines correspondent in the emission spectra.

**Source:** By the author.

By looking at the 500 shots correlation map shown in Figure 5.12 (a), we can see that the blue region enlarges once the band shift is even higher now, of about 3 nm. An interesting feature that appears in the correlation map is the region highlighted by the solid line square. This region becomes less correlated when compared to the map of the Figure 5.11 (a). If we

look this region in the emission spectra in Figure 5.12 (b), this phenomenon is related to the fact that the blueshift makes the band to vanishes in the 610 to 615 nm area in the spectra. So, those spectra which in this wavelengths are already just noise leads to a decreasing in the highlighted are of the correlation map.

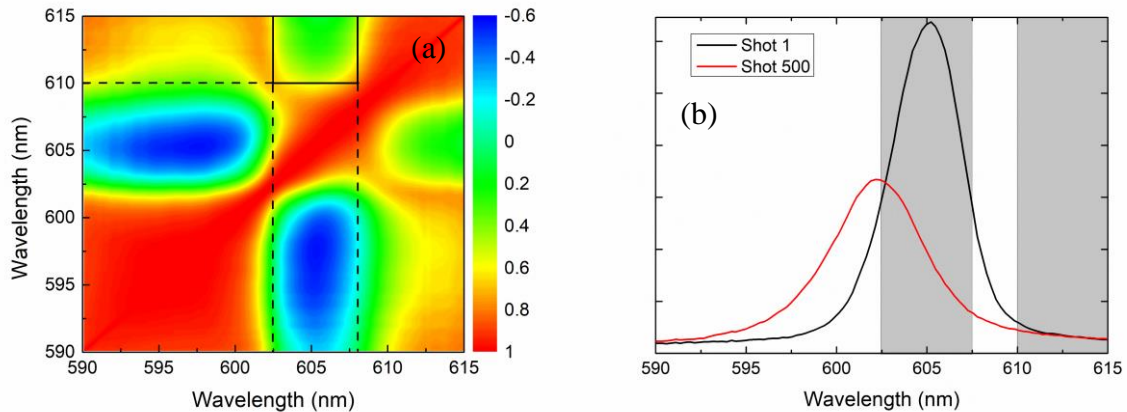


Figure 5.12: (a) Pearson correlation map of 500 shots. The area highlighted by the solid lines informs that a blue shift occurs. (b) The first and last emission spectra of a total of 500 shots. The grey regions are the same wavelength regions bounded by the dashed lines.

**Source:** By the author.

This is an attractive feature once now it is possible to distinguish in the map if the band is redshifting or blueshifting. Suppose that in another case, the red spectrum in Figure 5.12 (b) was instead redshifted. Now, the left part of the spectrum goes from intensity emission to just noise, for example, in the 595 to 600 nm. This would make the green region in the correlation map to appears in the lower left part of the map. So, when the green region happens to be in the upper right region, it represents a blueshift while a green region in the lower left region represents a redshift.

Summarizing, we can observe the evolution of the spectra in the five maps produced for each 100 shots made in Figure 5.13. It is possible to track both the widening and the bandshift. We can see the widening dynamics by monitoring the spreading of the blue region in the map and the blueshift by the arising of the green region in the upper right part of the map.

The application of the correlation map in a set of hundreds of spectra, until now only used to analyze incoherent to coherent transition in the random laser field as already mentioned in this thesis, could open a path to the idealization of a temperature or chemical sensors. That is, the effects that changed the pattern of the maps are due to sample heating, degradation of the host material or even some degradation of the organic dye caused by the successive pumping of the laser. But it is also possible to avoid the effect of the laser by setting a low value of

repetition rate and setting an energy pump just above the laser threshold. By doing so, the sample would only be sensitive to environment features. For instance, if the temperature of the environment changes, the correlation map would change and, given the fact that the change in the map occurs in extremely low changes in the spectrum, it could be a highly sensitive thermometer. Also, the emission is a laser-like one, enabling a high distance measurement just by adding a collimating lens in the system without the presence of an optical fiber. The temperature, in principal, could be read after each new pumping of the sample. For a 10 Hz repetition rate laser pumping, we would have a new read of the temperature each 0.1 seconds.

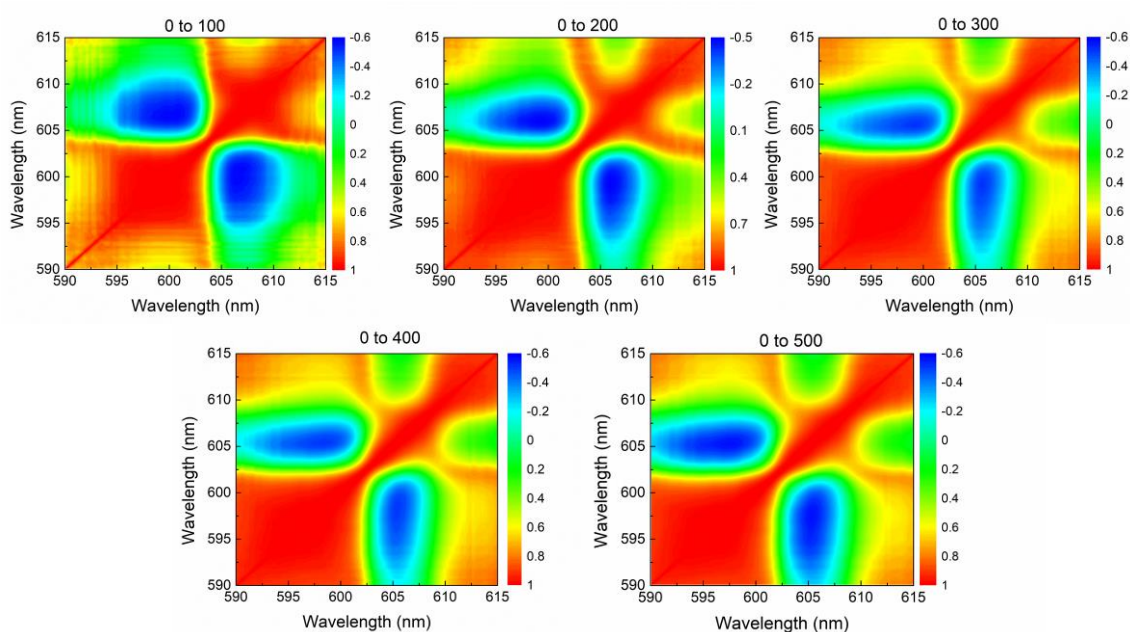


Figure 5.13: Pearson correlation map for an incoherent random laser emission from each 100 shots taken in 500 shots total.

**Source:** By the author.

For the chemical sensor, the proposal is having an ultra-sensitive sensor for gases. Suppose that the laser material is made of a polymer that is stable in normal conditions air but undergoes a degradation processes if some acid gas is presented in the air. The degradation leads to a changing in the sample morphology modifying the emission features and therefore, changing the correlation map.

## 5.4 Conclusions and perspectives

A Rhodamine B-doped polymeric nanofiber random laser produced via electrospinning technique was used to characterize a method of dynamically monitoring changes in a collection

of emission spectra acquired shot to shot of the pumping laser. The material is a series of randomly distributed fibers of approximately 500 nm in diameter, flexible and extremely thin, emitting random laser in 1  $\mu\text{J}$ /pulse energy threshold for a 5% (m/m) of Rhodamine B sample and 2.5  $\mu\text{J}$ /pulse energy threshold for a 1% (m/m) one. The random laser is promoted by the multiple scattering of light due to the randomly distributed nanofiber self-interlaced resulting of the fabrication technique itself.

By selecting a pumping spot in the sample, it was observed the same emission spectrum profile for uncorrelated pumping shots even though the light path from one pumping to another is completely random. But, also due to the randomly arranged fibers, the laser emission spectra for different pumping places in the sample are completely different from one another such a way that for a single sample, we can produce incoherent and coherent random laser. This feature made possible the mode-locking transition phenomenon, already shown in recent papers, but it is the first time that it could be done in a single sample, just by changing the place we are exciting.

One of the features to analyze the mode-locking transition is calculating the Pearson correlation coefficient in both incoherent and coherent cases by doing a mapping of all the coefficient in the wavelengths comprising the emission spectrum. In this work, we propose a new application of the correlation map. By producing a set of maps from time to time of spectra acquisition, it is a more sensitive way to monitor the changes in the laser emission, been possible to track line widening, blue or redshift or even the arising or vanishing of a certain mode in coherent laser emission.

For further investigations, we are willing to test those sensor features in real tests, such as temperature changes calibrating a temperature scale and use some gas in a controlled atmosphere to observe how the correlation maps evolve as a function of the gas concentration and even obtain a degradation threshold. Those experiments could reveal this technique to be a highly sensitive thermal and chemical sensor.

It is worth noticing that this method concerns changing the samples morphology or dye degradation to monitor the dynamical variation of the emission spectra. Therefore, it could also be used to track reactions of the samples itself. For instance, suppose a liquid random laser and a substance used to start its solidification. While the solidification is taking place, a series of correlation maps can be performed in order to observe the laser modes behavior in a coherent random laser or a bandshift and band widening in an incoherent one. This is also true for dye degradation or quenching.

In summary, the correlation maps could be used to see any dynamical process happening in the sample that affects the laser emission, it could be a change in the sample environment or in the sample morphology itself. The advantage of this method is that if the emission band changes is too small for spectrum-to-spectrum comparison, it yet can be observed in the correlation map. If the process is too fast, we could still produce a map by acquiring spectra in 0.1 seconds or even in less time if we have a high repetition rate pumping laser. Also, the analyzes itself is much faster and carries more information of the emission changes than analyzing it one by one.

## REFERENCES

1. Maiman, T. H. Stimulated optical radiation in Ruby. *Nature* **187**, 493–494 (1960).
2. Schäfer, F. P., Schmidt, W. & Volze, J. Organic dye solution laser. *Appl. Phys. Lett.* **9**, 306–309 (1966).
3. Javan, A., Bennett, W. R. & Herriott, D. R. Population Inversion and Continuous Optical Maser Oscillation in a Gas Discharge Containing a He-Ne Mixture. *Phys. Rev. Lett.* **6**, 106–110 (1961).
4. Jeong, Y., Sahu, J. K., Payne, D. N. & Nilsson, J. Ytterbium-doped large-core fiber laser with 1.36 kW continuous-wave output power. *Opt. Express* **12**, 6088 (2004).
5. Chang, S.-W. *et al.* A White Random Laser. *Sci. Rep.* **8**, 2720 (2018).
6. Siegman, A. E. *Lasers*. (University Science Books, 1986).
7. Myers, T. D. & McDaniel, J. D. The pulsed Nd:YAG dental laser: review of clinical applications. *J. Calif. Dent. Assoc.* **19**, 25–30 (1991).
8. Wachulak, P. W., Marconi, M. C., Bartels, R. A., Menoni, C. S. & Rocca, J. J. Soft x-ray laser holography with wavelength resolution. *J. Opt. Soc. Am. B* **25**, 1811 (2008).
9. Clark, J. & Lanzani, G. Organic photonics for communications. *Nat. Photonics* **4**, 438–446 (2010).
10. Silfvast, W. T. *Laser fundamentals*. (Cambridge University Press, 2004).
11. Schäfer, F. P. Principles of Dye Laser Operation. in 1–85 (1973). doi:10.1007/978-3-662-11579-4\_1
12. Letokhov, V. S. Generation of light by a scattering medium with negative resonance absorption. *Sov. Phys. JETP* **26**, 835–840 (1968).
13. Lawandy, N. M., Balachandran, R. M., Gomes, A. S. L. & Sauvain, E. Laser action in strongly scattering media. *Nature* **368**, 436–438 (1994).
14. Cao, H. *et al.* Random Laser Action in Semiconductor Powder. *Phys. Rev. Lett.* **82**, 2278–2281 (1999).
15. Turitsyn, S. K. *et al.* Random distributed feedback fibre laser. *Nat. Photonics* **4**, 231–235 (2010).
16. Liu, J. *et al.* Random nanolasing in the Anderson localized regime. *Nat. Nanotechnol.* **9**, 285–289 (2014).
17. Tulek, A., Polson, R. C. & Vardeny, Z. V. Naturally occurring resonators in random lasing of  $\pi$ -conjugated polymer films. *Nat. Phys.* **6**, 303–310 (2010).
18. García-Revilla, S. *et al.* Ultrafast random laser emission in a dye-doped silica gel powder. (2008).
19. Zhang, J. *et al.* Random lasing and weak localization of light in transparent Nd<sup>+3</sup> doped phosphate glass. *Appl. Phys. Lett.* **102**, 21109 (2013).
20. Tomazio, N. B., Sciuti, L. F., de Almeida, G. F. B., De Boni, L. & Mendonca, C. R. Solid-state random microlasers fabricated via femtosecond laser writing. *Sci. Rep.* **8**, 13561 (2018).

21. Redding, B., Choma, M. A. & Cao, H. Speckle-free laser imaging using random laser illumination. *Nat. Photonics* **6**, 355–359 (2012).
22. Redding, B., Liew, S. F., Sarma, R. & Cao, H. Compact spectrometer based on a disordered photonic chip. *Nat. Photonics* **7**, 746–751 (2013).
23. Wan Ismail, W. Z., Liu, G., Zhang, K., Goldys, E. M. & Dawes, J. M. Dopamine sensing and measurement using threshold and spectral measurements in random lasers. *Opt. Express* **24**, A85-91 (2016).
24. Polson, R. C. & Vardeny, Z. V. Random lasing in human tissues. *Appl. Phys. Lett.* **85**, 1289–1291 (2004).
25. Perumbilavil, S. *et al.* Beaming random lasers with soliton control. *Nat. Commun.* **9**, 3863 (2018).
26. Yuan, F. *et al.* Ultrastable and Low-Threshold Random Lasing from Narrow-Bandwidth-Emission Triangular Carbon Quantum Dots. *Adv. Opt. Mater.* **7**, 1801202 (2019).
27. Anderson, B. R., Gunawidjaja, R. & Eilers, H. Low-Threshold and Narrow Linewidth Diffusive Random Lasing in Rhodamine 6G Dye-Doped Polyurethane with Dispersed ZrO<sub>2</sub> Nanoparticles. *J. Opt. Soc. Am. B* **31**, 2363–2370 (2014).
28. Zhu, H. *et al.* Low-threshold GaN thin-film random laser through the weak scattering feedback. *J. Phys. D: Appl. Phys.* **50**, 45107 (2017).
29. Wiersma, D. Laser physics: The smallest random laser. *Nature* **406**, 132–135 (2000).
30. Saleh, B. E. A. & Teich, M. C. *Fundamentals of photonics*. (Wiley-Interscience, 2007).
31. Verdeyen, J. T. *Laser electronics*. (Prentice Hall, 1995).
32. Drake, J. M., Morse, R. I., Steppel, R. N. & Young, D. Kiton red S and rhodamine B. The spectroscopy and laser performance of red laser dyes. *Chem. Phys. Lett.* **35**, 181–188 (1975).
33. van Soest, G. Experiments on random laser. (2001).
34. Wiersma, D. S. The physics and applications of random lasers. *Nat. Phys.* **4**, 359–367 (2008).
35. van de Hulst, H. C. Light Scattering by Small Particles. *Light Scatt. by Small Part. New York John Wiley Sons, 1957* **1**, 470 (1957).
36. Feynman, R. P. Radiation damping and light scattering. in *The Feynman Lectures on Physics* (1963).
37. Ambartsumyan, R. V., Basov, N. G., Kryukov, P. G. & Letokhov, V. S. A laser with nonresonant feedback. *Sov. Phys. JETP* **24**, 481–485 (1967).
38. Genack, A. Z. & Drake, J. M. Scattering for super-radiation. *Nature* **368**, 400–401 (1994).
39. Frolov, S. V., Vardeny, Z. V., Yoshino, K., Zakhidov, A. & Baughman, R. H. Stimulated emission in high-gain organic media. *Phys. Rev. B* **59**, R5284–R5287 (1999).
40. Cao, H. *et al.* Investigation of random lasers with resonant feedback. *Am. Phys. Soc. Annu. APS March Meet. March 18 - 22, 2002 Indiana Conv. Center; Indianapolis, Indiana Meet. ID MAR02, Abstr. id. G8.007* (2002).

41. Cao, Xu, Chang & Ho. Transition from amplified spontaneous emission to laser action in strongly scattering media. *Phys. Rev. E. Stat. Phys. Plasmas. Fluids. Relat. Interdiscip. Topics* **61**, 1985–9 (2000).
42. Wiersma, D. S., Bartolini, P., Lagendijk, A. & Righini, R. Localization of light in a disordered medium. *Nature* **390**, 671–673 (1997).
43. Cao, H. *et al.* Spatial Confinement of Laser Light in Active Random Media. *Phys. Rev. Lett.* **84**, 5584–5587 (2000).
44. Vanneste, C. & Sebbah, P. Selective Excitation of Localized Modes in Active Random Media. *Phys. Rev. Lett.* **87**, 183903 (2001).
45. Jiang, X. & Soukoulis, C. M. Time Dependent Theory for Random Lasers. *Phys. Rev. Lett.* **85**, 70–73 (2000).
46. Apalkov, V. M., Raikh, M. E. & Shapiro, B. Random Resonators and Prelocalized Modes in Disordered Dielectric Films. *Phys. Rev. Lett.* **89**, 16802 (2002).
47. Polson, R. C. & Vardeny, Z. V. Organic random lasers in the weak-scattering regime. *Phys. Rev. B* **71**, 45205 (2005).
48. Polson, R. C., Raikh, M. E. & Vardeny, Z. V. Universal properties of random lasers. *IEEE J. Sel. Top. Quantum Electron.* **9**, 120–123 (2003).
49. Wilhelmi, B. Laser action in resonators composed of scattering mesoscopic particles. in (eds. Akos, G., Lupkovics, G. & Podmaniczky, A.) **3573**, 13 (International Society for Optics and Photonics, 1998).
50. Herrmann, J. & Wilhelmi, B. Mirrorless laser action by randomly distributed feedback in amplifying disordered media with scattering centers. *Appl. Phys. B Lasers Opt.* **66**, 305–312 (1998).
51. Mujumdar, S., Ricci, M., Torre, R. & Wiersma, D. S. Amplified Extended Modes in Random Lasers. *Phys. Rev. Lett.* **93**, 53903 (2004).
52. Cao, H. *et al.* Ultraviolet lasing in resonators formed by scattering in semiconductor polycrystalline films. *Appl. Phys. Lett.* **73**, 3656 (1998).
53. Wu, X. & Cao, H. Statistical studies of random-lasing modes and amplified spontaneous-emission spikes in weakly scattering systems. *Phys. Rev. A* **77**, 13832 (2008).
54. Wu, X., Andreasen, J., Cao, H. & Yamilov, A. Effect of local pumping on random laser modes in one dimension. *J. Opt. Soc. Am. B* **24**, A26 (2007).
55. Arruda, T. J. Espalhamento de ondas eletromagnéticas por esferas e cilindros magnéticos. (University of São Paulo, 2010).
56. Hulst, H. C. van de. *Light scattering by small particles*. (Dover Publications, 1981).
57. Bohren, C. F. & Huffman, D. R. *Absorption and scattering of light by small particles*. (John Wiley & Sons, Ltd, 1983).
58. Lagendijk, A. & van Tiggelen, B. A. *Resonant multiple scattering of light*. *Physics Reports* **270**,

- (1996).
59. Lee Rodgers, J. & Nicewander, W. A. Thirteen Ways to Look at the Correlation Coefficient. *Am. Stat.* **42**, 59–66 (1988).
  60. Pearson, K. Note on Regression and Inheritance in the Case of Two Parents. *Proc. R. Soc. London* **58**, 240–242 (1895).
  61. Neto, A. M. *et al.* *Image Processing Using Pearson's Correlation Coefficient: Applications on Autonomous Robotics*. (2013).
  62. Kozak, M., Krzanowski, W. & Tartanus, M. Use of the correlation coefficient in agricultural sciences: problems, pitfalls and how to deal with them. *An. Acad. Bras. Cienc.* **84**, 1147–1156 (2012).
  63. Leonetti, M., Conti, C. & Lopez, C. The mode-locking transition of random lasers. *Nat. Photonics* **5**, 615–617 (2011).
  64. Inkson, B. J. Scanning electron microscopy (SEM) and transmission electron microscopy (TEM) for materials characterization. *Mater. Charact. Using Nondestruct. Eval. Methods* 17–43 (2016). doi:10.1016/B978-0-08-100040-3.00002-X
  65. Goldstein, J. *et al.* *Scanning electron microscopy and x-ray microanalysis*. (Plenum Publishers, 2003).
  66. Binnig, G., Quate, C. F. & Gerber, C. Atomic Force Microscope. *Phys. Rev. Lett.* **56**, 930–933 (1986).
  67. Haugstad, G. *Atomic force microscopy : understanding basic modes and advanced applications*. (John Wiley & Sons, Ltd, 2012).
  68. Gross, L., Mohn, F., Moll, N., Liljeroth, P. & Meyer, G. The chemical structure of a molecule resolved by atomic force microscopy. *Science (80- )*. **325**, 1110–1114 (2009).
  69. Meng, X., Fujita, K., Murai, S. & Tanaka, K. Coherent random lasers in weakly scattering polymer films containing silver nanoparticles. *Phys. Rev. A* **79**, 53817 (2009).
  70. Caixeiro, S., Gaio, M., Marelli, B., Omenetto, F. G. & Sapienza, R. Silk-Based Biocompatible Random Lasing. *Adv. Opt. Mater.* **4**, 998–1003 (2016).
  71. Marinho, S. J. *et al.* Bi-chromatic random laser from alumina porous ceramic infiltrated with rhodamine B. *Laser Phys. Lett.* **12**, 55801 (2015).
  72. Judeinstein, P. & Sanchez, C. Hybrid organic–inorganic materials: a land of multidisciplinary. *J. Mater. Chem.* **6**, 511–525 (1996).
  73. Altman, J. C., Stone, R. E., Dunn, B. & Nishida, F. Solid-state laser using a rhodamine-doped silica gel compound. *IEEE Photonics Technol. Lett.* **3**, 189–190 (1991).
  74. Wen, J. & Wilkes, G. Organic/Inorganic Hybrid Network Materials by the Sol–Gel Approach. *Chem. Mater.* **8**, 1667–1681 (1996).
  75. Hench, L. L. & West, J. K. The sol-gel process. *Chem. Rev.* **90**, 33–72 (1990).
  76. Brinker, C. J. & Scherer, G. W. *Sol-gel science : the physics and chemistry of sol-gel processing*.

- (Academic Press, 1990).
77. Abegão, L. M. G. *et al.* Random laser emission from a Rhodamine B-doped GPTS/TEOS-derived organic/silica monolithic xerogel. *Laser Phys. Lett.* **14**, 65801 (2017).
  78. Yokota, T. *et al.* Ultraflexible organic photonic skin. *Sci. Adv.* **2**, e1501856 (2016).
  79. Visentin, F., Fiorini, P. & Suzuki, K. A Deformable Smart Skin for Continuous Sensing Based on Electrical Impedance Tomography. *Sensors* **16**, 1928 (2016).
  80. Sun, T.-M. *et al.* Stretchable Random Lasers with Tunable Coherent Loops. *ACS Nano* **9**, 12436–12441 (2015).
  81. Hu, H.-W. *et al.* Wrinkled 2D Materials: A Versatile Platform for Low-Threshold Stretchable Random Lasers. *Adv. Mater.* **29**, 1703549 (2017).
  82. Ignesti, E. *et al.* A new class of optical sensors: a random laser based device. *Sci. Rep.* **6**, 35225 (2016).
  83. Choi, S. H. & Kim, Y. L. The potential of naturally occurring lasing for biological and chemical sensors. *Biomed. Eng. Lett.* **4**, 201–212 (2014).
  84. Montinaro, M. *et al.* Diverse Regimes of Mode Intensity Correlation in Nanofiber Random Lasers through Nanoparticle Doping. *ACS Photonics* **5**, 1026–1033 (2018).
  85. Sugavanam, S., Sorokina, M. & Churkin, D. V. Spectral correlations in a random distributed feedback fibre laser. *Nat. Commun.* **8**, 15514 (2017).
  86. El-Dardiry, R. G. S., Mosk, A. P., Muskens, O. L. & Lagendijk, A. Experimental studies on the mode structure of random lasers. *Phys. Rev. A* **81**, 43830 (2010).
  87. Merrill, J. W., Cao, H. & Dufresne, E. R. Fluctuations and correlations of emission from random lasers. *Phys. Rev. A* **93**, 21801 (2016).
  88. Li, D. & Xia, Y. Electrospinning of Nanofibers: Reinventing the Wheel? *Adv. Mater.* **16**, 1151–1170 (2004).
  89. Huang, Z.-M., Zhang, Y.-Z., Kotaki, M. & Ramakrishna, S. A review on polymer nanofibers by electrospinning and their applications in nanocomposites. *Compos. Sci. Technol.* **63**, 2223–2253 (2003).
  90. Mercante, L. A., Scagion, V. P., Migliorini, F. L., Mattoso, H. C. & Correa, D. S. Electrospinning-based (bio)sensors for food and agricultural applications: A review. *Trends Anal. Chem.* **91**, 91–103 (2017).
  91. Thenmozhi, S., Dharmaraj, N., Kadirvelu, K. & Kim, Y. Electrospun nanofibers: New generation materials for advanced applications. *Mater. Sci. Eng. B* **217**, 36–48 (2017).
  92. Ye, L. *et al.* Study of low-threshold and high-intensity random lasing in dye doped liquid crystals. *J. Laser Appl.* **28**, 22005 (2016).
  93. Okamoto, T. & Yoshitome, R. Random lasing in dye-doped polymer random media with a bubble structure. *J. Opt. Soc. Am. B* **34**, 1497 (2017).
  94. Casey, K. G. & Quitevis, E. L. Effect of solvent polarity on nonradiative processes in xanthene

dyes: Rhodamine B in normal alcohols. *J. Phys. Chem.* **92**, 6590–6594 (1988).

## Appendix A – LabView program to calculate the correlation coefficient

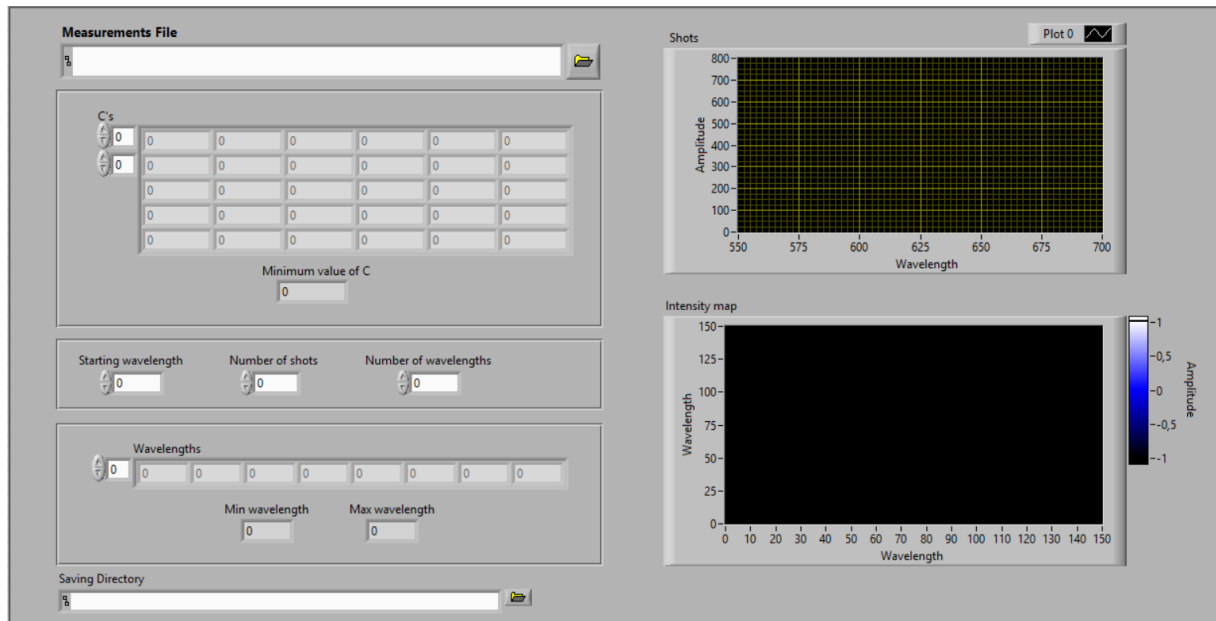


Figure A.1: Front end of the program to produce the correlation coefficient map.

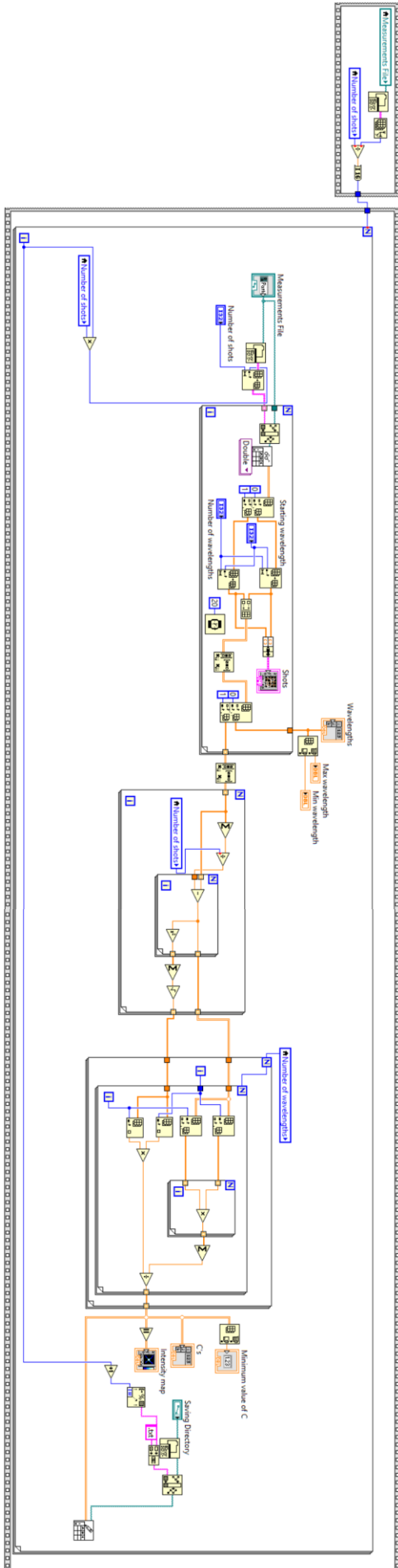


Figure A.1 shows the front end of the program of the correlation map calculation. In the left column, there is the table of C values that will result the 2D graph and the wavelengths and number of spectra inputs. In the upper right, the spectrum that is performing the calculations are shown. In the bottom right, the resultant correlation map is depicted. The user can set a file directory where a .txt file with the table of C values are saved.

Figure A.2 shows the block diagram where the programming is made in LabView. From left to right, the processes are: open and read the file with all the emission spectra cutting the unnecessary wavelengths; get the intensity values of each wavelength for all the spectra; perform the parts of the calculation of the Pearson correlation equation that refers to only one wavelength; finish the Pearson coefficient calculation by multiplying and summing by pairing all the possible pairs of wavelengths; Output the C values and the correlation map and save the C table in a .txt file.

Figure A.2: Block diagram of the program used to perform the correlation maps.

## Appendix B – Publications in Journal Papers

### Published papers

- 1) T. S. Gonçalves, J. F. M. Dos Santos, **L. F. Sciuti**, T. Catunda and A. S. S. De Camargo, “Thermo-optical spectroscopic investigation of new Nd<sup>3+</sup>-doped fluoro-aluminophosphate glasses,” *J. Alloys Compd.*, vol. 732, pp. 887–893, 2018.
- 2) N. B. Tomazio, **L. F. Sciuti**, G. F. B. de Almeida, L. De Boni and C. R. Mendonca, “Solid-state random microlasers fabricated via femtosecond laser writing,” *Sci. Rep.*, vol. 8, no. 1, p. 13561, Dec. 2018.
- 3) **L. F. Sciuti**, L. H. Z. Cocca, A. R. L. Caires, P. J. Gonçalves and L. De Boni, “Picosecond dynamic of aqueous sodium-copper chlorophyllin solution: An excited state absorption study,” *Chem. Phys. Lett.*, vol. 706, pp. 652–657, 2018.
- 4) L. H. Z. Cocca, F. Gotardo, **L. F. Sciuti**, T. V Acunha, B. A. Iglesias and L. De Boni, “Investigation of excited singlet state absorption and intersystem crossing mechanism of isomeric meso-tetra(pyridyl)porphyrins containing peripheral polypyridyl platinum(II) complexes,” *Chem. Phys. Lett.*, vol. 708, pp. 1–10, 2018.
- 5) F. R. Henrique *et al.*, “Luz à primeira vista: um programa de atividades para o ensino de óptica a partir de cores,” *Rev. Bras. Ensino Física*, vol. 41, no. 3, pp. 1–7, 2019.

### In submission process

- 1) **L. F. Sciuti**, T. S. Gonçalves, N. B. Tomazio, A. S. S. de Camargo, C. R. Mendonça and L. De Boni, “Random laser action in dye-doped xerogel with inhomogeneous TiO<sub>2</sub> nanoparticles distribution.” *Journal of Materials Science: Materials in Electronics*.
- 2) L. H. Z. Cocca, **L. F. Sciuti**, *et. al.*, “Shield effect in the excited sates of meso-mono-substituted (amino-ferrocenyl) porphyrins: Experimental and theoretical approaches.” *Physical Chemistry Chemical Physics*.

Presentations in conferences: 4 international and 6 national.